Effect of pore size distribution on sorption-induced deformation of porous materials: a theoretical study

Mehdi Eskandari-Ghadi[1] and Yida Zhang[2]

ABSTRACT

Porous materials exhibit complex deformation when interacting with adsorbates in the environment. Depending on the size and shape of individual pores, interactions between solid and adsorbates can give rise to several pore-scale forces that impacts the overall adsorption and strain isotherms. Accurate prediction of the adsorption-deformation behavior of a porous material would benefit from the consideration of its pore network characteristics described by the pore size distribution (PSD). This paper presents a theoretical investigation on how the pore size distribution can affect the sorption-induced deformation of micro/meso/macro porous solids. The recently developed surface poromechanics theory is generalized to account for the information of arbitrary pore size distributions. The adsorptive energetics of a generic pore network is statistically upscaled from the solid-adsorbate interaction in a single slit pore geometry, which is then infused into the thermodynamics of a deformable body. The theory is first validated against the experimental data on microporous carbon interacting with nitrogen gas. Then the same parameter set is used to study the effects of pore size on the adsorption and strain isotherms of porous materials. By only varying the input PSDs, a variety of adsorption-deformation behaviors that are commonly observed from experiments is reproduced by the model. Conclusions are drawn from this analysis regarding the relative dominance of different pore-scale forces at varying pore size ranges, and the circumstances where simplified representation of the pore network can be acceptable.

KEYWORDS

Poromechanics, Adsorption, Pore size distribution, Swelling/shrinkage

[1] Postdoctoral Associate, Department of Civil, Environmental and Architectural Engineering, University of Colorado Boulder, Boulder, CO, USA.
[2] Assistant professor, Department of Civil, Environmental and Architectural Engineering, University of Colorado Boulder, Boulder, CO, USA. Email: yida.zhang@colorado.edu

1 INTRODUCTION

The coupling between adsorption and deformation in porous solids has long intrigued engineers and materials scientists (Bangham and Fakhoury, 1928; Gor et al., 2017; Lakhanpal and Flood, 1957). During adsorption, fluid molecules (adsorbate) spontaneously gathers and structuralizes near a solid surface (adsorbent) (Rahaman et al., 2008). The occurrence of such process in a porous network can exert stresses onto the solid skeleton and thus induce volumetric strain with magnitude ranging from 10^{-3} for charcoal (Balzer et al., 2015) and porous glass (Amberg and McIntosh, 1952), to tens of percent for silica aerogels (Reichenauer and Scherer, 2001), clay (Lyu et al., 2015), polymeric fibers (Champeau et al., 2014), and cellulose (Chen et al., 2018), and up to hundreds of percent for metal-organic frameworks (Serre et al., 2007). Nature takes advantage of such stimuli-responsive feature of cellulose nanofibers to facilitate the dispersal of plant seeds upon humidity change (Dawson et al., 1997; Elbaum et al., 2007; Van Opdenbosch et al., 2016). Bio-inspired nanoporous networks have been recently developed for fast and reliable actuators (Zhao et al., 2014), gas sensors muscles (Lee et al., 2019), and artificial (Yang et al., 2018) driven by sorption of gas molecules. On the other hand, adsorption/desorption can negatively impact the health of structural materials by triggering cracking (Colina and Roux, 2000), degradation (Baek and Pence, 2009) and plastic deformation (Hansen, 1987). For the ubiquitousness of sorption-induce deformation, it is crucial to pursue fundamental mechanistic understanding of such phenomenon in generic fluid - porous solid systems.

Various porous materials exhibit drastically different adsorption and strain isotherms. They can be roughly categorized in three types: Early experiments on charcoal show monotonic expansion upon gas uptake (Type I behavior as sketched in Fig. 1), which was explained by the decrease of pore surface energy due to adsorption (also known as the *Bangham effect*) (Bangham and Fakhoury, 1928; Meehan, 1927). Later, Haines and McIntosh (1947) and Lakhanpal and Flood (1957) studied activated microporous carbon and found that a small amount of volumetric shrinkage occurs at extremely low pressure regime before Bangham's expansion (Type II behavior as sketched in Fig. 1). This was attributed to an attractive "bridging" of adsorbate molecules from one side of the pore wall to the opposing side. Amberg and McIntosh (1952) studied the interaction between mesoporous Vycor glass and water vapor and observed two distinct expansion segments, separated by a contraction regime in the intermediate pressure range, on the adsorption strain isotherm (Type III behavior as sketched in Fig. 1). The contraction was related to Laplace pressure caused by concave menisci formed during condensation

(Amberg and McIntosh, 1952; Haines and McIntosh, 1947; Wiig and Juhola, 1949). A forth type of behavior can be also be observed when both initial contraction and capillary contraction occur (Balzer et al., 2015). After 1970s, numerous in-situ dilatometer tests have been conducted on other porous materials including zeolites (Fomkin, 2005), porous silicon (Dolino et al., 1996), biopolymers (Rey and Vandamme, 2013), aerogel (Reichenauer and Scherer, 2001), natural coal (Levine, 1996), shale (Heller and Zoback, 2014), and cement (Setzer and Wittmann, 1974). Their strain isotherms can be all categorized as one of the four types. Our hypothesis here is that the different types of strain isotherms are tightly associated with the adsorbent's pore structures. For example, the "bridging" in Lakhanpal and Flood's notion is only possible for pore size of nanometers, giving rise to the so-called disjoining pressure (de Feijter, 1988) that is largely attractive at low pressures (Ash et al., 1973). This effect is recently quantitatively studied in a continuum poromechanics setting and shown to create an overall contractive stress on the pore skeleton (Eskandari-Ghadi and Zhang, 2021). On the other hand, mesoporous materials have pores large enough that meniscus can develop upon capillary condensation (El Tabbal et al., 2020). Materials that have a wide range of pore sizes or dual porosity networks may co-exhibit initial contraction and condensation contraction (Balzer et al., 2015).

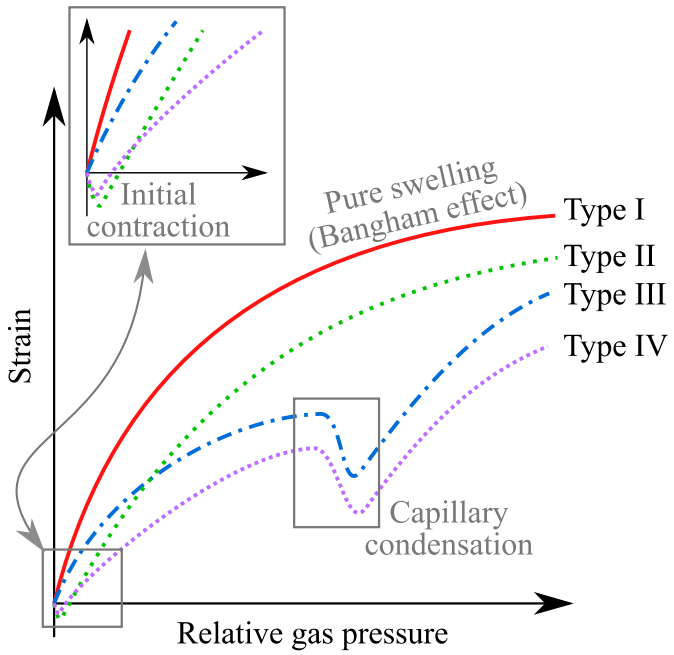

Fig. 1. Schematic of categorization of adsorption-deformation behavior.

Quantitative simulation of the adsorption-deformation process requires proper consideration of the underlying physics. Molecular simulations based on approximation of particle-particle interactions can

reasonably capture pore-scale and even meso-scale processes. In particular, such simulations have demonstrated the variation of disjoining pressure with respect to changing gas pressure and pore size (Kowalczyk et al., 2008), swelling and contraction upon capillary condensation and adsorption hysteresis (Chen et al., 2019), and initial contraction based on disjoining pressure calculations (Kowalczyk et al., 2012). Density functional theory simulations have also provided insights on adsorption and strain correlation at a molecular level (Ravikovitch and Neimark, 2006) and two-way coupling of adsorption and deformation (Gor and Bernstein, 2016). On the other hand, poromechanics which incorporates the mechanical interactions of solids and fluids at macroscale (Coussy, 2004) allows one to efficiently obtain the response of a continuum with spatially variable properties, arbitrary boundary conditions, and coupled with time-dependent processes (e.g. diffusion) at low computational cost. Such an efficient and versatile tool for engineering analysis, however, is only as accurate as the underlying pore-scale physics that the constitutive models incorporate. For example, the classical poromechanical framework laid out by Biot (1941) and Coussy (2010) considered the effect of fluid pressure exerted on the pore walls and the compressibility of the solid phase in describing the response of inert, saturated porous media. Recent advances have elegantly accounted for several pore-scale mechanisms to reproduce adsorption straining in mesopores and micropores (Brochard et al., 2012b; Eskandari-Ghadi and Zhang, 2021; Pijaudier-Cabot et al., 2011; Vandamme et al., 2010; Zhang, 2018). Pijaudier-Cabot et al. (2011) have attempted to integrate the information of pore network in the macroscale modeling of porous media. Brochard et al. (2012a) have performed one-dimensional molecular simulations to study the two-way adsorption-deformation coupling in a uniform and random distribution of pore sizes. However, there are no systematic theoretical studies unveiling the effect of pore size distribution on the distinct adsorption-deformation characteristics of porous continua to the best of our knowledge.

To address the above, the current work is presented with two main objectives: (1) put forward a continuum framework that accounts for the change of surface tension and disjoining pressure upon gas uptake in pores with various sizes, and (2) study the influence of pore size distribution on the adsorption strain isotherms under the proposed framework, in hoping to clarify the transition between the type I and type II behaviors. Capturing the Type III and IV behaviors requires the incorporation of capillary condensation at pore scale, which is beyond the scope of this paper and will be pursued elsewhere. In this aspiration, the thermodynamics of a generic adsorptive pore network is established based on that of a single slit pore and then integrated with the kinematics of a deformable body in Section 2 . After

linearizing the constitutive equation, the framework is cast into incremental form to acquire versatility and simplicity in its numerical implementation in Section 3 . In Section 4 , an explicit adsorption-deformation model is obtained by specifying proper poroelasticity, microstructure, and adsorption models, which is then subjected to validation against experimental data of N_2 adsorption on microporous carbon in Section 5 . Finally, systematic parametric studies on the effect of pore size distribution on the characteristics of sorption strain isotherm are presented in Section 6 .

2 SURFACE POROMECHANICS: FROM INDIVIDUAL PORES TO THE POROUS MEDIUM

When guest molecules (adsorbate) approach to internal pore surface of a porous medium (adsorbent), they are influenced by surface forces such as van der Waals force, electrostatic force and hydration forces (Israelachvili, 2011), modifying the properties of the solid-fluid interface. The resultant stresses exerted onto the pore surface can be studied in a thermodynamic setting which is detailed below. The IUPAC nomenclature is adopted throughout this paper: *micropore* denotes pore size less than 2 nm, *macropore* for sizes larger than 50 nm, and mesopore refers to everything in between (Everett, 1972).

Surface forces in a slit pore

Consider adsorption inside a slit pore. Some fluid molecules are in its “free” bulk state, while others are influenced by the surface force fields and thus in the structured and adsorbed state. In reality, there is no jump from one state to the other and their thermodynamic properties undergo a gradual transition. Details of such transition can be circumvented through the Gibbs’ surface excess treatment, permitting a much-simplified mathematical description of the energetics inside the pore. As illustrated in Fig. 2a, the Gibbs’ treatment defines a zero-thickness geometrical surface that lumps all the extensive properties inside the pore excess to the bulk fluid phase, thus accounting for fluid properties near the pore walls (DeHoff, 2006). The mere definition of such a surface phase gives rise to the notion of surface energy or surface tension, i.e., the thermodynamic force conjugated to the change of pore surface area (Zhang, 2018). For small enough confinements as represented in Fig. 2b, the interfacial regions of the opposing pore walls may overlap and interact. Such interaction may be described by an extra work necessary to change the distance between the two surfaces, which is additional to the work necessary to push the bulk fluid out of the pore. Inspired by the works of Rusanov (1966) and de Feijter (1988) on thin liquid films and consulting with the analysis of Ash et al. (1973), Eskandari-Ghadi and Zhang (2021) has recently considered the micropore system in Fig. 2b in terms of Gibbs’ excess convention and derived the expressions of *surface force* terms including disjoining pressure and surface tension inside a slit

111 micropore. However, the effects of the distributed pore sizes on the REV scale are smeared into the
112 adsorption-deformation of one or two average pores. An extension to the same line of thought is
113 presented in what follows for the consideration of an arbitrary number of pore sizes in the REV. The
114 internal energy of the surface phase for single-species adsorption in a slit pore can be written as
115 (Eskandari-Ghadi and Zhang, 2021)

116 $$d\tilde{U}^{surf} = Td\tilde{S}^{surf} - \frac{1}{2}\tilde{\mathcal{A}}\Pi dh + \gamma d\tilde{\mathcal{A}} + \mu d\tilde{N}^{surf} \tag{1}$$

117 where $\tilde{U}^{surf}$ is the internal energy of the surface phase; T is the system temperature; $\tilde{S}^{surf}$ is the entropy
118 of the surface phase; $\tilde{\mathcal{A}}$ is the total surface area available to adsorption; h is the thickness of the slit
119 pore; μ is the chemical potential of the adsorbate; $\tilde{N}^{surf}$ is the number of adsorbed moles to the surface
120 phase; γ is the surface tension, considered independent of the surface strain and to be distinguished
121 from the stretch-dependent surface stress (Kramer and Weissmüller, 2007); Π is the disjoining pressure
122 denoting the additional normal force per unit area generated by the overlapping of adsorbed regions of
123 two opposing pore walls (Fig. 2b) and is responsible for the deviation of actual pore pressure p^p from
124 the bulk fluid in micropores p (i.e., $\Pi = p^p - p$). Throughout this paper, we use superposed "tilde" to
125 denote extensive quantities pertaining to a single pore. Superscripts s, f, and $surf$ refer to quantities
126 belonging to the solid, the bulk fluid and the surface phases, respectively.

127 Eq. (1) can be re-written in terms of the volume of a single slit-pore, $\tilde{\Omega}^v = \tilde{\mathcal{A}}h/2$, as

128 $$d\tilde{U}^{surf} = Td\tilde{S}^{surf} - \Pi d\tilde{\Omega}^v + \gamma_p d\tilde{\mathcal{A}} + \mu d\tilde{N}^{surf} \tag{2}$$

129 where

130 $$\gamma_p = \gamma + \frac{1}{2}\Pi h \tag{3}$$

131 is referred to as the equivalent surface tension. The total form of the $\tilde{U}^{surf}$ can be achieved by
132 integrating Eq. (2) along a specific path in the variable space (Ash et al., 1973; Zhang, 2018). An
133 alternative way to obtain the total form of Eq. (2) is to recognize that $\tilde{U}^{surf}$ is a homogenous function of
134 degree one (de Feijter, 1988). Specifically, a system consisting of λ copies of the same pore must have
135 an internal energy of $\lambda\tilde{U}^{surf}$ with volume and surface area of $\lambda\tilde{\Omega}^v$ and $\lambda\tilde{\mathcal{A}}$, and entropy and number of

mole of $\lambda\tilde{S}^{surf}$ and $\lambda\tilde{N}^{surf}$. Invoking Euler's homogeneous function theorem readily gives us (Eskandari-Ghadi and Zhang, 2021):

$$\tilde{U}^{surf} = T\tilde{S}^{surf} - \Pi\tilde{\Omega}^{v} + \gamma_{p}\tilde{\mathcal{A}} + \mu\tilde{N}^{surf} \tag{4}$$

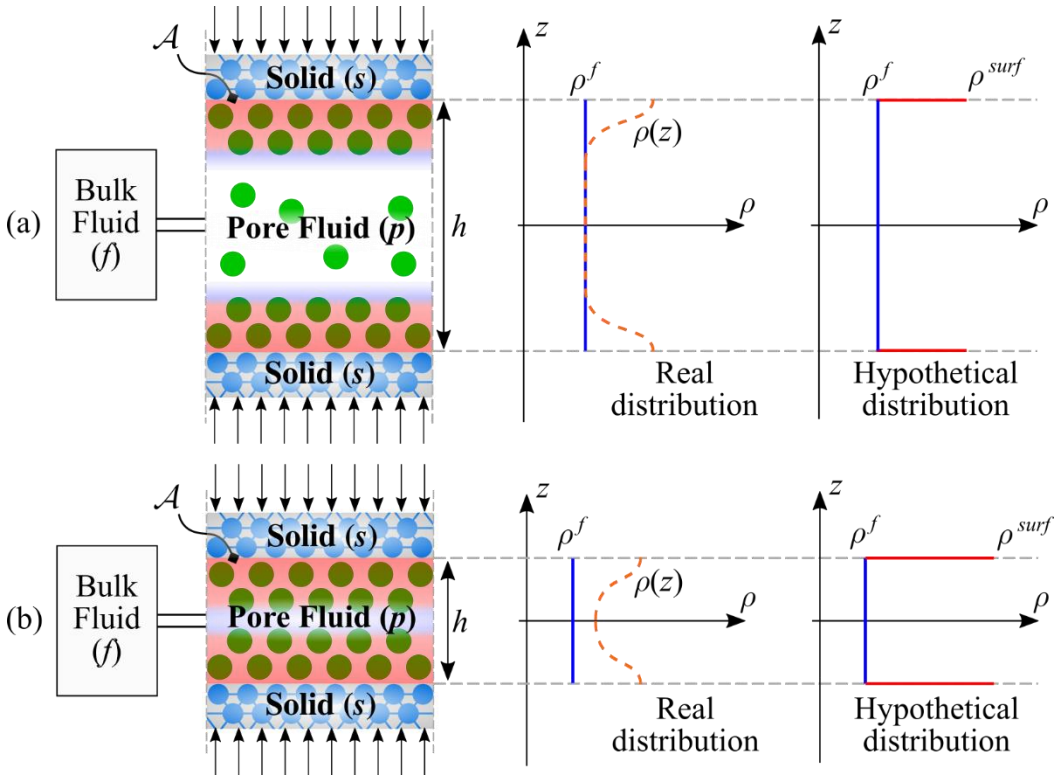

Fig. 2. Schematic of the Gibbs' surface excess treatment for a meso/macro pore in which the adsorbed regions do not overlap (a) and a micropore where the adsorbed regions overlap (b).

With the aid of Eq. (3), subtracting Eq. (2) from the total derivative of Eq. (4), and considering isothermal condition gives the surface tension increment (Ash et al., 1973)

$$d\gamma = -\Gamma d\mu - \frac{1}{2}\Pi dh \tag{5}$$

where $\Gamma = \tilde{N}^{surf}/\tilde{\mathcal{A}}$ is the surface excess concentration. Eq. (5) is a modification to the classical Gibbs' adsorption isotherm by considering the presence of an opposing wall with separation h. The Maxwell relation of Eq. (5) gives

$$\left.\frac{\partial\Pi}{\partial\mu}\right|_{h} = 2\left.\frac{\partial\Gamma}{\partial h}\right|_{\mu} \tag{6}$$

One may refer to Eskandari-Ghadi and Zhang (2021) for more detailed discussions of Eqs. (1) through (6). Assuming that the external gas reservoir can be described as ideal gas and invoking $d\mu = RTdp/p$, one can write the disjoining pressure increment:

$$d\Pi = \frac{2RT}{p}\frac{\partial \Gamma}{\partial h}dp + \frac{\partial \Pi}{\partial h}dh \tag{7}$$

Substituting Eq. (5) into the incremental form of Eq. (3) and considering Eq. (7) gives:

$$d\gamma_p = \frac{RT}{p}\left(-\Gamma + h\frac{\partial \Gamma}{\partial h}\right)dp + \frac{h}{2}\frac{\partial \Pi}{\partial h}dh \tag{8}$$

Eqs. (7) and (8) are the bases for computing the changes of surface forces (Π and γ_p) induced by adsorption via dp and nanoconfinement via dh. These effects then alter the stresses in the vicinity of individual pores and thus impact the macroscopic response of porous materials.

Alternatively, the energetics of the surface phase can be expressed in terms of the Helmholtz free energy by performing Legendre transformation of Eq. (2) with respect to T:

$$d\tilde{F}^{surf} = -\tilde{S}^{surf}dT - \Pi d\tilde{\Omega}^{v} + \gamma_p d\tilde{\mathcal{A}} + \mu d\tilde{N}^{surf} \tag{9}$$

Smeared surface forces in deformable porous skeleton

Consider a porous representative elementary volume (REV) in Fig. 3. It has volume Ω_0 at time $t = 0$, volume Ω and total pore surface area $\mathcal{A}$ at time t. The Lagrangian porosity and volume-specific area are defined as $\phi = \Omega^v/\Omega_0$ and $A_s = \mathcal{A}/\Omega_0$; respectively, where Ω^v is the total current pore volume. The initial pore volume is therefore $\Omega_0^v = \phi_0\Omega_0$, where ϕ_0 is the initial porosity. Let us further categorize the pores of the same size as the same "type" K which constitutes the fraction r_K of the total pore volume. The volume and surface area of pore group K are respectively written as $\Omega_K^v = r_K\Omega^v = r_K\phi\Omega_0 = \phi_K\Omega_0$ and $\mathcal{A}_K = A_{s,K}\Omega_0$, with $\sum_K r_K = 1$, $\sum_K \phi_K = \phi$, and $\sum_K A_{s,K} = A_s$. From here on, $\sum_K$ will be denoted by just $\sum$ for simplicity if not specified otherwise. We shall assume that each type of pore can be mapped to an equivalent slit pore which behaves similarly in terms of adsorption isotherm and surface forces. This allows us to associate the pore-scale thermodynamics of any pore

shape to that of a slit pore which is our building block derived in the previous section (see Section 4.2 for more discussions). Considering the system is thermally and chemically equilibrated everywhere and knowing that each pore group K consists of n_K copies of identical pores, the free energy increment of each pore group can be directly written from Eq. (9) as

$$dF_K^{surf} = -S_K^{surf} dT - \Pi_K d\Omega_K^v + \gamma_{p,K} d\mathcal{A}_K + \mu dN_K^{surf} \tag{10}$$

where $F_K^{surf} = n_K \tilde{F}_K^{surf}$, $S_K^{surf} = n_K \tilde{S}_K^{surf}$, $\Omega_K^{surf} = n_K \tilde{\Omega}_K^{surf}$, $\mathcal{A}_K^{surf} = n_K \tilde{\mathcal{A}}_K^{surf}$, and $N_K^{surf} = n_K \tilde{N}_K^{surf}$. According to Eqs. (7) and (8), the Maxwell relations between the intensive properties of each pore group are written as:

$$\left.\frac{\partial \Pi_K}{\partial p}\right|_{h_K} = \frac{2RT}{p}\left.\frac{\partial \Gamma_K}{\partial h_K}\right|_p, \quad \frac{\partial \gamma_{p,K}}{\partial p} = \frac{RT}{p}\left(-\Gamma_K + h_K \frac{\partial \Gamma_K}{\partial h_K}\right), \quad \frac{\partial \gamma_{p,K}}{\partial h_K} = \frac{h_K}{2}\frac{\partial \Pi_K}{\partial h_K} \tag{11}$$

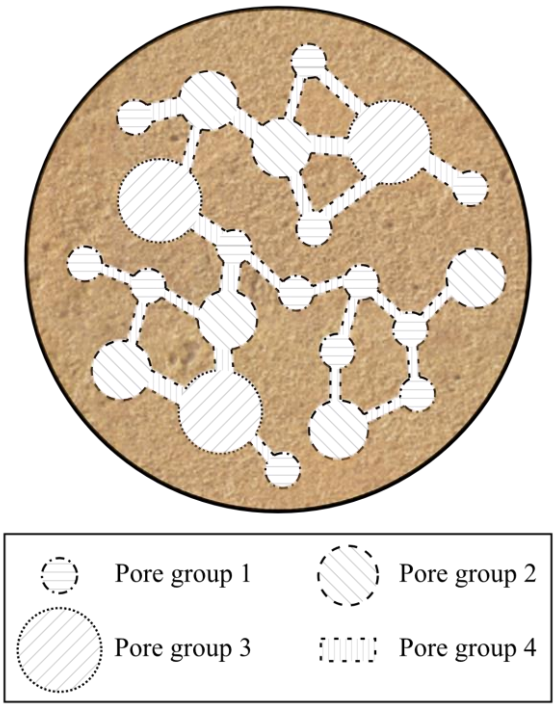

Fig. 3. Schematic of REV composition. The pore network is divided into four groups of identical pores. Each pore group consists of pores of the same *type* (i.e. size and shape).

Summing up the surface free energies of all pore groups from Eq. (10) gives the total free energy possessed by the surface phase of the entire REV:

186 $$dF^{surf} = -S^{surf}dT - \overbrace{\left(\sum \Pi_K \frac{\partial \Omega_K^v}{\partial \Omega^v}\right)}^{\bar{\Pi}} d\Omega^v + \overbrace{\left(\sum \gamma_{p,K} \frac{\partial \mathcal{A}_K}{\partial \mathcal{A}}\right)}^{\bar{\gamma}_p} d\mathcal{A} + \mu dN^{surf} \tag{12}$$

187 where $F^{surf} = \sum F_K^{surf}$, $S^{surf} = \sum S_K^{surf}$, and $N^{surf} = \sum N_K^{surf}$; $\bar{\gamma}_p$ and $\bar{\Pi}$ are respectively the smeared
188 equivalent surface tension and the smeared disjoining pressure that reflect the collective effect of surface
189 forces on the REV:

190 $$\bar{\gamma}_p = \sum \gamma_{p,K} \frac{\partial \mathcal{A}_K}{\partial \mathcal{A}} \text{ and } \bar{\Pi} = \sum \Pi_K \frac{\partial \Omega_K^v}{\partial \Omega^v} \tag{13}$$

191 Eq. (12) can be compared with Eq. (24) in Eskandari-Ghadi and Zhang (2021). Evidently, the smeared
192 surface forces in the multi-pore REV manifest in the same manner in the overall surface free energy
193 potential as those of the single-pore REV. Note that the surface tension is obtained by area averaging
194 while disjoining pressure is smeared over the pore volume.

195 The area-specific surface free energy, adsorbed moles, and entropy are then defined respectively as:

196 $$\psi^{surf} = F^{surf} / A_s\Omega_0,\ \Gamma = N^{surf} / A_s\Omega_0, \text{ and } s^{surf} = S^{surf} / A_s\Omega_0 \tag{14}$$

197 Using Eq. (14), the total surface free energy, Eq. (12), can be cast in terms of intensive quantities:

198 $$\begin{aligned} d\psi^{surf} &= -s^{surf}dT + \mu d\Gamma - \bar{\Pi}\frac{1}{A_s}d\phi + \left(\bar{\gamma}_p + \mu\Gamma - \psi^{surf}\right)\frac{1}{A_s}dA_s \\ &+ \frac{1}{\Omega_0}\left(\bar{\gamma}_p + \mu\Gamma - \psi^{surf} - \bar{\Pi}\frac{\phi}{A_s}\right)d\Omega_0 \end{aligned} \tag{15}$$

199 Eq. (15) must hold for an arbitrary domain $d\Omega_0$, thus the last term on the RHS must vanish

200 $$\psi^{surf} = \bar{\gamma}_p + \mu\Gamma - \bar{\Pi}\frac{\phi}{A_s} \text{ and } d\psi^{surf} = -s^{surf}dT + \mu d\Gamma - \bar{\Pi}d\left(\frac{\phi}{A_s}\right) \tag{16}$$

201 The second equation is essentially the specific free energy balance equation of the surface phase in a
202 porous REV.

203 The above derivations are conducted without considering the kinematics of the porous skeleton. Now
204 let us incorporate the energetics into a deformable body. Per the conventional continuum mechanics

notation, the motion of solid skeleton is described by $\mathbf{x}=\mathbf{x}(\mathbf{X},t)$, where $\mathbf{x}$ is the current spatial position of the solid particle at time t, and $\mathbf{X}$ is the position of the solid particle at time $t=0$. It follows the definition of deformation gradient $\mathbf{F}=\nabla_X\mathbf{x}$ and the Jacobian $J=\det\mathbf{F}$ which respectively map a line segment $d\mathbf{X}$ and a volume element $d\Omega_0$ in the reference configuration to the current configuration $d\mathbf{x}$ and $d\Omega$ via $d\mathbf{x}=\mathbf{F}\cdot d\mathbf{X}$ and $d\Omega=Jd\Omega_0$. By defining the displacement vector $\mathbf{u}^s=\mathbf{x}-\mathbf{X}$, the Green-Lagrange strain is written as $\mathbf{E}=\left(\nabla_X\mathbf{u}^s+{}^T\nabla_X\mathbf{u}^s+{}^T\nabla_X\mathbf{u}^s\cdot\nabla_X\mathbf{u}^s\right)/2$, where ∇_X denotes gradient with respect to material coordinate $\mathbf{X}$. Considering separately the mass, momentum, and energy balance of all phases and the interaction between the fluid and surface phase through adsorption, the Clausius-Duhem inequality of the system can be derived which gives the requirement of nonnegative material dissipation rate, $\Phi_M\geq 0$. The derivation is detailed in Zhang (2018) and Eskandari-Ghadi and Zhang (2021). The total material dissipation can be further decomposed into dissipation caused by changes of the states of the solid, the fluid, and the surface phases $\Phi_M=\Phi_M^s+\Phi_M^f+\Phi_M^{surf}$ guided by the free energy balance equations of each phase:

$$\Phi_M^s=\mathbf{S}:\frac{\partial\mathbf{E}}{\partial t}+\left(p+\bar{\Pi}\right)\frac{\partial\phi}{\partial t}-S^s\frac{\partial T}{\partial t}-\left(\rho^{surf}\hat{\psi}^{surf}-M\hat{\mu}^f\Gamma+\bar{\Pi}\frac{\phi}{A_s}\right)\frac{\partial A_s}{\partial t}-\frac{\partial\rho^s\left(J-\phi\right)\hat{\psi}^s}{\partial t} \tag{17}$$

$$\Phi_M^f=\rho^f\phi\left[-p\frac{\partial}{\partial t}\left(\frac{1}{\rho^f}\right)-\hat{s}^f\frac{\partial T}{\partial t}-\frac{\partial\hat{\psi}^f}{\partial t}\right] \tag{18}$$

$$\Phi_M^{surf}=A_s\left[M\hat{\mu}^f\frac{\partial\Gamma}{\partial t}-\rho^{surf}\hat{s}^{surf}\frac{\partial T}{\partial t}-\bar{\Pi}\frac{\partial}{\partial t}\left(\frac{\phi}{A_s}\right)-\frac{\partial\rho^{surf}\hat{\psi}^{surf}}{\partial t}\right] \tag{19}$$

where the superposed "hat" denotes mass-specific quantities; $\mathbf{S}$ the second Piola-Kirchhoff stress; ρ denotes density; M the molar mass of the fluid. For reversible processes, one can set $\Phi_M^{surf}=0$ and $\Phi_M^f=0$ to retrieve the free energy balance of the surface phase, Eq. (16), and the usual equations of state of the fluid phase (Coussy, 2004). Similarly, the free energy balance of adsorptive porous solid can be retrieved by considering $\Phi_M^s=0$, substituting Eq. (16) into Eq. (17), and adopting small-strain assumption:

$$d\Psi^s = \boldsymbol{\sigma} : d\boldsymbol{\varepsilon} + \left(p + \bar{\Pi} \right) d\phi - S^s dT - \bar{\gamma}_p dA_s \tag{20}$$

where $\boldsymbol{\sigma}$ and $\boldsymbol{\varepsilon}$ are the Cauchy stress tensor and infinitesimal strain tensor, respectively; Ψ^s is the free energy of the solid phase. Comparing Eq. (20) with the free energy balance of classical porous solid (Coussy, 2004), it is clear that adsorption influences the material behavior through the smeared surface force terms $\bar{\gamma}_p$ and $\bar{\Pi}$. It should be noted that although the alteration of the pore pressures $\bar{\Pi}$ arise from the short-range interactions inside pores of molecular length-scale (Fig. 2b), the surface tension $\bar{\gamma}_p$ exists regardless of the pore size (Coussy, 2010; Vandamme et al., 2010) which is responsible for the Bangham's effect. Finally, the choice of infinitesimal strain formulation is just for convenience, which is equivalent to focusing this study on relatively stiff porous skeletons. Eq. (17) can be directly used to theorize adsorption-induced finite deformations in soft porous materials if desired (see Zhang (2018)). Specific surface area must be a function of the kinematics of the REV, i.e., $A_{s,k}\left(\boldsymbol{\varepsilon}, \phi\right)$. Eq. (20) can thus be written as

$$d\Psi^s = \left(\boldsymbol{\sigma} - \bar{\gamma}_p \frac{\partial A_s}{\partial \boldsymbol{\varepsilon}} \right) : d\boldsymbol{\varepsilon} + \left(p + \bar{\Pi} - \bar{\gamma}_p \frac{\partial A_s}{\partial \phi} \right) d\phi \tag{21}$$

By specifying a strain-energy potential $\Psi^s\left(\boldsymbol{\varepsilon}, \phi\right)$, the constitutive relations for a deformable adsorptive porous material with a generic pore network are finally retrieved

$$\boldsymbol{\sigma} - \boldsymbol{\sigma}_a = \frac{\partial \Psi^s}{\partial \boldsymbol{\varepsilon}}; p - p_a = \frac{\partial \Psi^s}{\partial \phi} \tag{22}$$

where $\boldsymbol{\sigma}_a = \bar{\gamma}_p \partial A_s / \partial \boldsymbol{\varepsilon}$ and $p_a = -\bar{\Pi} + \bar{\gamma}_p \partial A_s / \partial \phi$ are adsorption stresses which collect the effect of adsorption on the "effective stresses" felted by the solid skeleton (Eskandari-Ghadi and Zhang, 2021; Gor et al., 2017; Ravikovitch and Neimark, 2006; Vandamme, 2019; Zhang, 2018). The theory is now completed. Constitutive models can be readily obtained by specifying the expressions of adsorption isotherm $\Gamma_K(p, h_K)$, the geometrical relation $A_{s,K}\left(\boldsymbol{\varepsilon}, \phi\right)$, and the strain-energy potential $\Psi^s\left(\boldsymbol{\varepsilon}, \phi\right)$.

3 INCREMENTAL FORM OF A GENERAL MODEL

Before specializing the theory for particular material systems, it is desirable to write the constitutive relation Eq. (22) in incremental form first. The primary reason is that Eq. (22) involves the derivatives of

A_s and the integral of $d\bar{\gamma}_p$ and $d\bar{\Pi}$ from Eqs. (7) and (8). The former can be easily computed having defined the $A_{s,K}(\boldsymbol{\varepsilon},\phi)$ function, while the analytical integration of $d\bar{\gamma}_p$ and $d\bar{\Pi}$ has some complications, especially if the adsorption isotherm $\Gamma_K(p,h_K)$ in Eq. (11) takes a sophisticated form. By casting the constitutive relations in incremental form, we can discretize these integrations in the stepwise stress-strain solutions and thus circumvent the direct numerical evaluations of the surface force terms. Besides, the incremental form also allows us to modularize the numerical solver such that the constitutive components Γ, A_s, and Ψ^s can be easily swapped upon desire. This makes the theory versatile to handle a wide range of porous materials with different physical and geometrical properties.

Consider a quadratic form of Ψ^s which corresponds to a general linear poroelastic model

$$\Psi_s = \left[\frac{\mathbf{C}^{\varepsilon}}{2}:\left(\boldsymbol{\varepsilon}-\boldsymbol{\varepsilon}_r\right)\right]:\left(\boldsymbol{\varepsilon}-\boldsymbol{\varepsilon}_r\right)+\mathbf{C}^{\varepsilon\phi}:\left(\boldsymbol{\varepsilon}-\boldsymbol{\varepsilon}_r\right)\left(\phi-\phi_r\right)+\frac{C^{\phi}}{2}\left(\phi-\phi_r\right)^2 \tag{23}$$

where the symmetric fourth-rank tensor $\mathbf{C}^{\varepsilon}$, the symmetric second-rank tensor $\mathbf{C}^{\varepsilon\phi}$, and the scalar C^{ϕ}, are the "stiffness coefficients"; $\left(\boldsymbol{\varepsilon}_r,\phi_r\right)$ is an arbitrary reference state. Substitution of Eq. (23) into Eq. (22) gives:

$$\begin{aligned}\boldsymbol{\sigma}-\Delta\left(\bar{\gamma}^p\frac{\partial A_s}{\partial\boldsymbol{\varepsilon}}\right)&=\mathbf{C}^{\varepsilon}:\boldsymbol{\varepsilon}+\mathbf{C}^{\varepsilon\phi}\left(\phi-\phi_0\right)\\ p+\Delta\bar{\Pi}-\Delta\left(\bar{\gamma}^p\frac{\partial A_s}{\partial\phi}\right)&=\mathbf{C}^{\varepsilon\phi}:\boldsymbol{\varepsilon}+C^{\phi}\left(\phi-\phi_0\right)\end{aligned} \tag{24}$$

In deriving Eq. (24) we have taken the stress-free state ($\boldsymbol{\varepsilon}=\mathbf{0}$ and $\phi=\phi_0$) in vacuum as the reference state (Eskandari-Ghadi and Zhang, 2021). The Δ symbol denotes the changes of the adsorption stresses, $\boldsymbol{\sigma}_a$ and p_a, from vacuum to the current environment. By differentiating Eq. (24), the incremental form is acquired and can be written in indicial notation as

$$\begin{aligned}d\sigma_{ij}-d\left(\bar{\gamma}_p\frac{\partial A_s}{\partial\varepsilon_{ij}}\right)&=C^{\varepsilon}_{ijkl}d\varepsilon_{kl}+C^{\varepsilon\phi}_{ij}d\phi\\ dp+d\bar{\Pi}-d\left(\bar{\gamma}_p\frac{\partial A_s}{\partial\phi}\right)&=C^{\varepsilon\phi}_{kl}:d\varepsilon_{kl}+C^{\phi}d\phi\end{aligned} \tag{25}$$

Recalling from Eqs. (7), (8), and (11) that the surface forces are functions of p and h_K, and noting that the pore size h_K is functions of global deformation $\boldsymbol{\varepsilon}$ and ϕ in a general case, Eq. (25) can be expanded and reorganized to give the stress and pressure increments (see Appendix A for full details):

$$d\sigma_{ij} = \left(C^{\varepsilon}_{ijkl} + C^{ads,\sigma\varepsilon}_{ijkl}\right) d\varepsilon_{kl} + \left(C^{\varepsilon\phi}_{ij} + C^{ads,\sigma\phi}_{ij}\right) d\phi \tag{26}$$

$$dp = \frac{1}{H}\left(C^{\varepsilon\phi}_{kl} + C^{ads,p\varepsilon}_{kl}\right) d\varepsilon_{kl} + \frac{1}{H}\left(C^{\phi} + C^{ads,p\phi}\right) d\phi \tag{27}$$

where

$$H = 1 - \frac{\partial \overline{\gamma}_p}{\partial p}\frac{\partial A_s}{\partial \phi} + \frac{\partial \overline{\Pi}}{\partial p} \tag{28}$$

$$C^{ads,p\varepsilon}_{kl} = \frac{\partial \overline{\gamma}_p}{\partial \varepsilon_{kl}}\frac{\partial A_s}{\partial \phi} + \Delta\overline{\gamma}_p \frac{\partial^2 A_s}{\partial \varepsilon_{kl}\partial \phi} - \frac{\partial \overline{\Pi}}{\partial \varepsilon_{kl}} \tag{29}$$

$$C^{ads,p\phi} = \frac{\partial \overline{\gamma}_p}{\partial \phi}\frac{\partial A_s}{\partial \phi} + \Delta\overline{\gamma}_p \frac{\partial^2 A_s}{\partial \phi^2} - \frac{\partial \overline{\Pi}}{\partial \phi} \tag{30}$$

$$C^{ads,\sigma\varepsilon}_{ijkl} = \frac{1}{H}\frac{\partial \overline{\gamma}_p}{\partial p}\frac{\partial A_s}{\partial \varepsilon_{ij}}\left(C^{\varepsilon\phi}_{kl} + C^{ads,p\varepsilon}_{kl}\right) + \frac{\partial \overline{\gamma}_p}{\partial \varepsilon_{kl}}\frac{\partial A_s}{\partial \varepsilon_{ij}} + \Delta\overline{\gamma}_p \frac{\partial^2 A_s}{\partial \varepsilon_{kl}\partial \varepsilon_{ij}} \tag{31}$$

$$C^{ads,\sigma\phi}_{ij} = \frac{1}{H}\frac{\partial \overline{\gamma}_p}{\partial p}\frac{\partial A_s}{\partial \varepsilon_{ij}}\left(C^{\phi} + C^{ads,p\phi}\right) + \frac{\partial \overline{\gamma}_p}{\partial \phi}\frac{\partial A_s}{\partial \varepsilon_{ij}} + \Delta\overline{\gamma}_p \frac{\partial^2 A_s}{\partial \phi\partial \varepsilon_{ij}} \tag{32}$$

The smeared quantities in Eqs. (28)-(32) are given by

$$\Delta\overline{\gamma}_p = \sum \Delta\gamma_{p,K}\frac{\partial \mathcal{A}_K}{\partial \mathcal{A}} \tag{33}$$

$$\frac{\partial \overline{\gamma}_p}{\partial p} = \sum \frac{\partial \gamma_{p,K}}{\partial p}\frac{\partial \mathcal{A}_K}{\partial \mathcal{A}} \tag{34}$$

$$\frac{\partial \overline{\gamma}_p}{\partial \varepsilon_{kl}} = \sum \frac{\partial \gamma_{p,K}}{\partial h_K}\frac{\partial h_K}{\partial \varepsilon_{kl}}\frac{\partial \mathcal{A}_K}{\partial \mathcal{A}} + \sum \Delta\gamma_{p,K}\frac{\partial}{\partial \varepsilon_{kl}}\frac{\partial \mathcal{A}_K}{\partial \mathcal{A}} \tag{35}$$

$$\frac{\partial \bar{\gamma}_p}{\partial \phi} = \sum \frac{\partial \gamma_{p,K}}{\partial h_K} \frac{\partial h_K}{\partial \phi} \frac{\partial \mathcal{A}_K}{\partial \mathcal{A}} + \sum \Delta\gamma_{p,K} \frac{\partial}{\partial \phi} \frac{\partial \mathcal{A}_K}{\partial \mathcal{A}} \tag{36}$$

$$\frac{\partial \bar{\Pi}}{\partial p} = \sum \frac{\partial \Pi_K}{\partial p} \frac{\partial \Omega_K^v}{\partial \Omega^v} \tag{37}$$

$$\frac{\partial \bar{\Pi}}{\partial \varepsilon_{kl}} = \sum \frac{\partial \Pi_K}{\partial h_K} \frac{\partial h_K}{\partial \varepsilon_{kl}} \frac{\partial \Omega_K^v}{\partial \Omega^v} \tag{38}$$

$$\frac{\partial \bar{\Pi}}{\partial \phi} = \sum \frac{\partial \Pi_K}{\partial h_K} \frac{\partial h_K}{\partial \phi} \frac{\partial \Omega_K^v}{\partial \Omega^v} \tag{39}$$

Evaluating Eq. (33)-(39) requires $\Delta\gamma_{p,K}$ and several derivatives $\partial\Omega_K^v / \partial\Omega^v$, $\partial\mathcal{A}_K / \partial\mathcal{A}$, $\partial\left(\partial\mathcal{A}_K / \partial\mathcal{A}\right) / \partial\phi$, and $\partial\left(\partial\mathcal{A}_K / \partial\mathcal{A}\right) / \partial\varepsilon_{ij}$. The change of $\gamma_{p,K}$ at each solution step can be computed from Eq. (11)

$$d\gamma_{p,K} = \left[\frac{1}{H}\left(C_{kl}^{\varepsilon\phi} + C_{kl}^{ads,p\varepsilon}\right)\frac{\partial \gamma_{p,K}}{\partial p} + \frac{\partial \gamma_{p,K}}{\partial h_K}\frac{\partial h_K}{\partial \varepsilon_{kl}}\right] d\varepsilon_{kl} + \left[\frac{1}{H}\left(C^{\phi} + C^{ads,p\phi}\right)\frac{\partial \gamma_{p,K}}{\partial p} + \frac{\partial \gamma_{p,K}}{\partial h_K}\frac{\partial h_K}{\partial \phi}\right] d\phi \tag{40}$$

Assuming that each pore group takes up a constant volume fraction of the total pore volume throughout deformation, we have $\partial\Omega_K^v / \partial\Omega^v = r_K$ where r_K is now constant. The derivatives of $\mathcal{A}_K$ and $\mathcal{A}$ are obtained in Appendix B based on their definitions.

4 SPECIALIZATION OF THE MODEL

In order to validate the theory with experimental data, one must specify proper constitutive components according to the material of interest. Balzer et al. (2015) have conducted a series of experiments on microporous carbon specimens interacting with different gas species and reported the adsorption isotherms as well as the induced strains. This offers a comprehensive dataset for validating the theory. Here we specialize the current model for the microporous carbon used in their experiments.

Poroelasticity model

Since there is no information about the three-dimensional response of the microporous carbon specimens in Balzer et al. (2015), the isotropic linear poroelasticity model (Coussy, 2004) seems appropriate for a first-order description:

306 $$C^{\varepsilon}_{ijkl} = \left(K - 2G/3 + b^2 N\right)\delta_{ij}\delta_{kl} + G\left(\delta_{ik}\delta_{jl} + \delta_{il}\delta_{jk}\right),\ C^{\varepsilon\phi}_{ij} = -bN\delta_{ij}, \text{ and } C^{\phi} = N \quad (41)$$

307 where K and G are the bulk and shear moduli of the specimen in absence of fluid, respectively; b and
308 N are the Biot's coefficient and Biot's modulus, respectively.

309 ***Microstructure: spherical pores***

310 The specimens are characterized by a network of pores presented in Fig. 4. While Balzer et al.
311 (2015) have obtained the pore size distribution using analysis based on slit pores for the micropores and
312 cylindrical pores for the mesopores, their analysis of SEM imaging suggests spherical pores. Here, for
313 simplicity, the same PSD data is assumed for a network of approximately spherical pores of different
314 sizes. Assuming the pores undergo isotropic change in size and thus shrinking or expanding only in
315 radius, the volume-specific surface area of a spherical pore group can be derived as (Zhang, 2018)

316 $$A_{s,K} = \frac{3}{R_{K,0}}\phi_{K,0}^{1/3}\phi_K^{2/3} \quad (42)$$

317 where $R_{0,K}$ is the initial radius of spheres of type K. Based on the definition of Ω_K^v, $\phi_K = r_K\phi$ and
318 having already assumed that the volume fractions remain constant, we have $\phi_K = r_K\phi$ and $\phi_{K,0} = r_K\phi_0$.
319 Thus Eq. (42) becomes

320 $$A_{s,K} = \frac{3r_K}{R_{K,0}}\phi_0^{1/3}\phi^{2/3} \quad (43)$$

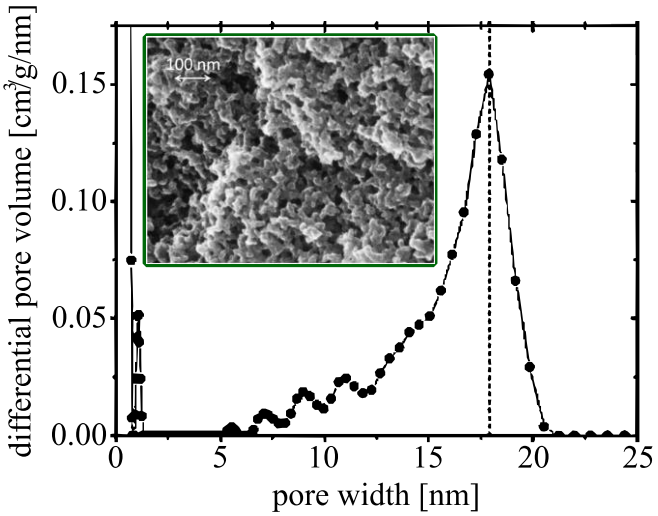

321

Fig. 4. Pore size distribution of the activated charcoal specimen studied by Balzer et al. (2015). The sub-figure is an SEM image of the sample. Based on the image, it seems that a network of interconnected spheres may be suitable to represent the specimen pore network.

Eq. (43) implies $\partial A_{s,K} / \partial \varepsilon_{ij} = 0$ which significantly simplifies Eqs. (29), (31), and (32).

Another geometrical function needs to be defined is $h_K = h_K(\boldsymbol{\varepsilon}, \phi)$. To map the adsorption behavior of a spherical pore to its equivalent slit pore, the pore radius and its equivalent slit opening are proposed to be related by $h_K = \alpha_K(R_K) R_K$. It is further assumed that the changes in pore size and shape are sufficiently small such that they have an overall negligible effect on the adsorption characteristics, giving a first order approximation of the geometry $h_K = \alpha R_{K,0}$. An intuitive way to derive the mapping factor α is to set the volume of the spherical pore, $\Omega^v_{K,0} = 4\pi R^3_{K,0} / 3 = \mathcal{A}_{K,0} R_{K,0} / 3$, equal to the equivalent slit pore volume, $h_K \mathcal{A}_{K,0} / 2$, giving $\alpha = 2/3$:

$$h_K = \frac{2}{3} R_{K,0} \tag{44}$$

The mathematical consequence of Eq. (44) is that the equivalent slit-pore width of each pore type become frozen (i.e., $\partial h_K / \partial \varepsilon_{ij} = \partial h_K / \partial \phi = 0$). This implies that the adsorption isotherm is independent of the material deformation and thus focuses the current study on the adsorption-induced deformation rather than the two-way coupling. This is consistent with our earlier assumption that the adsorption isotherm is independent of surface stretch for the relatively stiff materials interested here. These treatments allow for tangible numerical integration of the model without losing the generality of the theory for tackling the two-way coupled mechanosorptive behaviors in future extensions. In particular, the frozen h_K assumption breaks down for highly deformable materials where the pore sizes can change drastically, for example in breathable Metal Organic Frameworks (MOFs) (Coudert et al., 2013) and polymers (Chen et al., 2020). Further enrichments of the model using constitutive functions like $h_K = \alpha_K(R_K) R_K$ and $\Gamma_K(p, h_K, \varepsilon_A)$ (where ε_A is the surface strain) are required if the theory is applied to highly deformable adsorptive materials.

Using Eqs. (43) and (44), the incremental constitutive relation Eqs. (26)-(39) are now simplified to:

$$d\sigma_{ij} = C^{\varepsilon}_{ijkl} d\varepsilon_{kl} + C^{\varepsilon\phi}_{ij} d\phi \tag{45}$$

$$dp = \frac{1}{H} C_{kl}^{\varepsilon\phi} d\varepsilon_{kl} + \frac{1}{H}\left(C^{\phi} + C^{ads,p\phi}\right) d\phi \tag{46}$$

where

$$H = 1 - \frac{\partial A_s}{\partial \phi} \sum \frac{\partial \gamma_{p,K}}{\partial p} \frac{\partial \mathcal{A}_K}{\partial \mathcal{A}} + \sum \frac{\partial \Pi_K}{\partial p} \frac{\partial \Omega_K^v}{\partial \Omega^v} \tag{47}$$

$$C^{ads,p\phi} = \frac{\partial A_s}{\partial \phi} \sum \gamma_{p,K} \frac{\partial \mathcal{A}_K}{\partial \mathcal{A} \partial \phi} + \frac{\partial^2 A_s}{\partial \phi^2} \sum \gamma_{p,K} \frac{\partial \mathcal{A}_K}{\partial \mathcal{A}} \tag{48}$$

$$\frac{\partial \mathcal{A}_K}{\partial \mathcal{A}} = \frac{\partial A_{s,K}}{\partial \phi} \frac{1}{\sum \frac{\partial A_{s,K}}{\partial \phi}} \tag{49}$$

$$\frac{\partial}{\partial \phi} \frac{\partial \mathcal{A}_K}{\partial \mathcal{A}} = \frac{\partial^2 A_{s,K}}{\partial \phi^2} \frac{1}{\sum \frac{\partial A_{s,K}}{\partial \phi}} - \frac{\partial A_{s,K}}{\partial \phi} \frac{\sum \frac{\partial^2 A_{s,K}}{\partial \phi^2}}{\left(\sum \frac{\partial A_{s,K}}{\partial \phi}\right)^2} \text{ and } \frac{\partial}{\partial \varepsilon_{ij}} \frac{\partial \mathcal{A}_K}{\partial \mathcal{A}} = 0 \tag{50}$$

Adsorption model

For meso/macro porous materials, adsorption can be considered to occur on free solid surfaces and thus modelled by either Langmuir (Langmuir, 1918) or the BET (Brunauer et al., 1938) isotherms. However, the specimen studied by Balzer et al. (2015) contains more than twenty percent volume of micropores (< 2 nm) (Fig. 4), thus a significant amount of adsorbed gas molecules are constrained by the surrounding pore walls (Fig. 1b), making the adsorption isotherm a function of both fluid pressure and pore size. This aspect has been studied by Brunauer et al. (1940), who applied the same stochastic procedure used to derive the BET model on a slit-pore geometry. Their derived adsorption model, here referred to as the BDDT isotherm, can be written as

$$\frac{\Gamma(n,x)}{\Gamma_0} = \frac{cx}{1-x} \cdot \left\{ \frac{1 + \left(\frac{ng}{2} - n\right) x^{n-1} - \left(ng - n + 1\right) x^n + \frac{ng}{2} x^{n+1}}{1 + \left(c-1\right) x + \left(\frac{cg}{2} - c\right) x^n - \frac{cg}{2} x^{n+1}} \right\} \tag{51}$$

where Γ_0 is some reference moles per unit area; $x = p / p_0$ is the ratio of gas pressure over the saturation pressure. The maximum number of adsorbed layers that can fit between the two surfaces are

$2n-1$ (Brunauer et al., 1940). Here we assume n is proportional to the height of the slit pore by $n = C_h h$, where C_h is a proportionality factor, for simplicity and to be consistent with the previous study (Eskandari-Ghadi and Zhang, 2021). Parameters c and g are related to characteristics energies $c \approx \exp(\Delta E / (RT))$ and $g = \exp(Q / (RT))$ (Brunauer et al., 1940; Brunauer et al., 1938); R is the ideal gas constant; ΔE is the difference between the energy to bond a fluid layer to a solid surface and the energy to bond a fluid layer to a fluid layer; Q is the additional heat necessary to "push" the last layer of molecules between the two adsorbed surfaces. Hereafter ΔE and Q will be referred to as the *adsorption energy* and the *additional adsorption heat*, respectively. The surface forces, γ_p and Π, predicted by the BDDT model combined with Eq. (11) are discussed in detail in Eskandari-Ghadi and Zhang (2021). The variation of normalized surface forces $\Delta\tilde{\gamma}_p = \Delta\gamma_p / 2RT\Gamma_0$ and $\Delta\tilde{\Pi} = \Delta\Pi / 2RT\Gamma_0 C_h$ with respect to fluid pressure and pore width are presented in Fig. 5a and Fig. 5b, along with the resultant normalized adsorption pressure $\Delta\tilde{p}_a$ in Fig. 5c. It is observed that surface tension reduces for all pore sizes and pressures as expected. At small pore size and low pressures, the attractive disjoining pressure wins over the relaxation of surface tension and creates a positive adsorption pressure which leads to material contraction. Outside of this region, the reduction of surface tension dominates and produces a negative adsorption pressure to cause swelling.

It is worth to note that the disjoining pressure derived from BDDT model is a lumped and smooth representation of the surface interactions between two solid surfaces in the given fluid environment. Molecular-scale simulations (Balbuena et al., 1993; Grégoire et al., 2018) and direct surface force measurements (Israelachvili, 2011) showed that the disjoining pressure is highly oscillatory when it comes down to nanometer separations. For the macroscopic modeling of porous materials, however, we argue that such oscillatory feature of disjoining pressure is secondary and can be neglected. Specifically, consider two nanopores with similar size h but have tiny size variations. Their true disjoining pressures might be drastically different in magnitude and sign because of the oscillation. However, there are thousands of such pores in a porous REV, and the overall disjoining pressure in pores with similar size h must be the averaged value around that size. For this reason, a smooth representation of Π is preferred for the later continuum modeling of microporous materials.

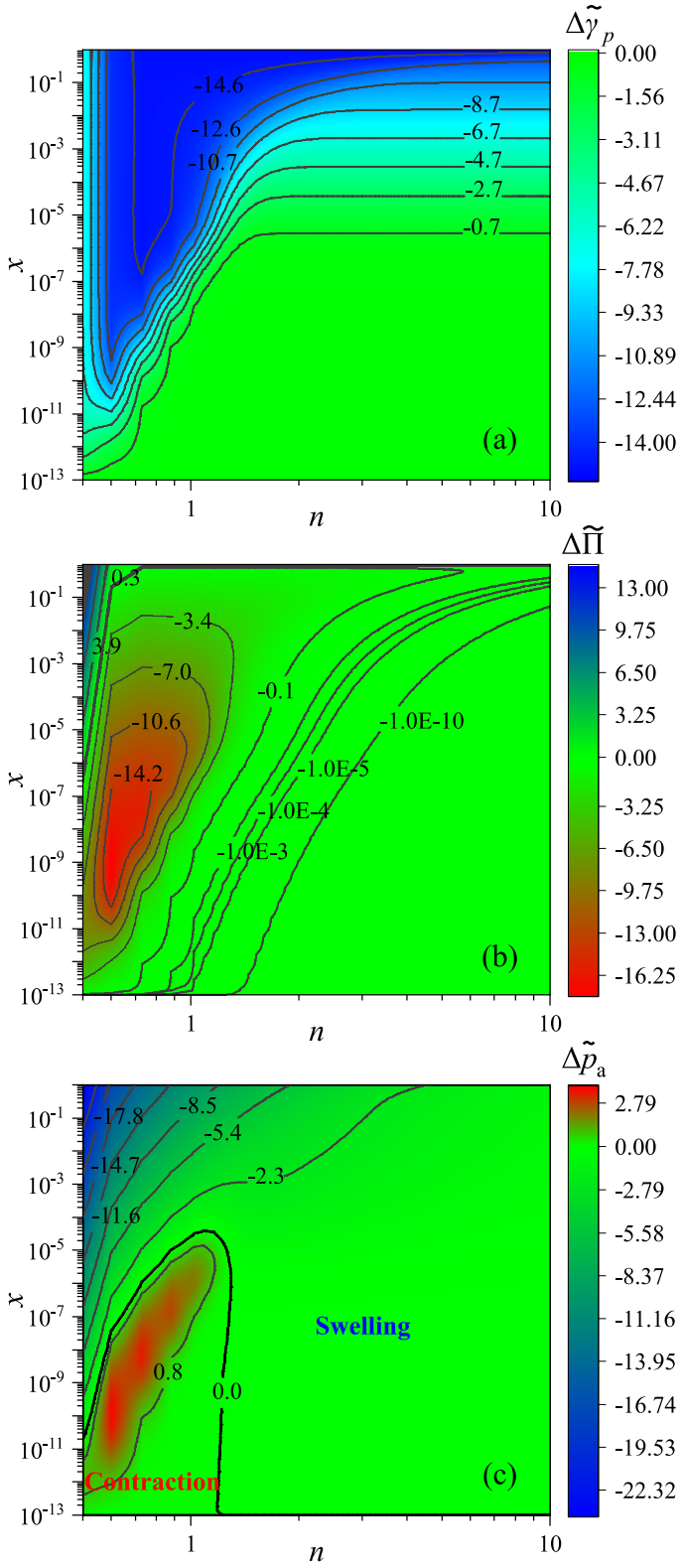

Fig. 5. Contours of the dimensionless equivalent surface tension (a), disjoining pressure (b), and resultant dimensionless adsorption pressure ($\Delta\tilde{p}_a = \Delta p_a / 2RT\Gamma_0 C_h$) (c) produced from the BDDT theory (Eq. (51)) and Eq. (11). The input parameters to the BDDT model are $\Delta E = 1940\text{cal/mol}$ and $Q = 440\text{cal/mol}$.

5 MODEL PERFORMANCE

With definitions of the stiffness coefficients in Eq. (41), the microstructure model in Eqs. (43) and (44), and the adsorption model in Eq. (51), we have introduced eight model parameters including K, ν, b, N, ΔE, Q, Γ_0, and C_h, all of which are physically meaningful and can be measured through routine experiments. The inputs of the model include: the adsorbate's saturation pressure p_0 and molar volume V_m, the adsorbent's specific gravity G_s and initial porosity ϕ_0, the system's temperature T, the sphere-slit mapping factor α, and the PSD information r_K and $R_{K,0}$. In what follows, we assign the experimentally obtained PSD and calibrate the material parameters for microporous carbon to validate the theory against the dataset of Balzer et al. (2015).

PSD discretization

For PSD input, the discrete differential PSD data provided by Balzer et al. (2015) is first represented by several continuous basis functions in the normal distribution form (Fig. 6a)

$$P(D/D_0) = \frac{1}{w\sqrt{2\pi}} e^{-\frac{1}{2}\left(\frac{D/D_0 - m}{w}\right)^2} \tag{52}$$

where $P(D/D_0)$ is the differential pore volume percentage; D the pore diameter for spherical pores; D_0 = 1 nm is a normalization parameter to keep parameters m and w unitless; $D_0 m$ is the peak pore width; w controls the "width" of the distribution. The number of basis functions is chosen to coincide with the number of peaks in the PSD data. A weighted sum of the seven bases is used to capture PSD as well as to ensure the total area underneath equals to 1. The theoretical PSD (in percentage) is then multiplied by the total pore volume per grams of material $0.86\ \mathrm{cm}^3/\mathrm{g}$ to compare with the experimental data (in volume per gram of the solid). The cumulative PSD can be obtained by integrating the differential PSD. The results are illustrated in Fig. 6b and c with the parameters summarized in Table 1.

Based on the fitted PSD curve in Fig. 6, the pore volume fractions (PVF) corresponding to individual pore sizes can be deduced. The pore widths are discretized into 107 bins (class intervals). These bins are refined (0.02 nm in width) in the microporous range and coarser (0.2 nm in width) in the mesoporous range. We have verified that further decrease of the bin sizes does not make significant difference in the

predicted material response. The final PSD discretization is presented in Fig. 7. Of course, the volume fractions of all bins sum to unity.

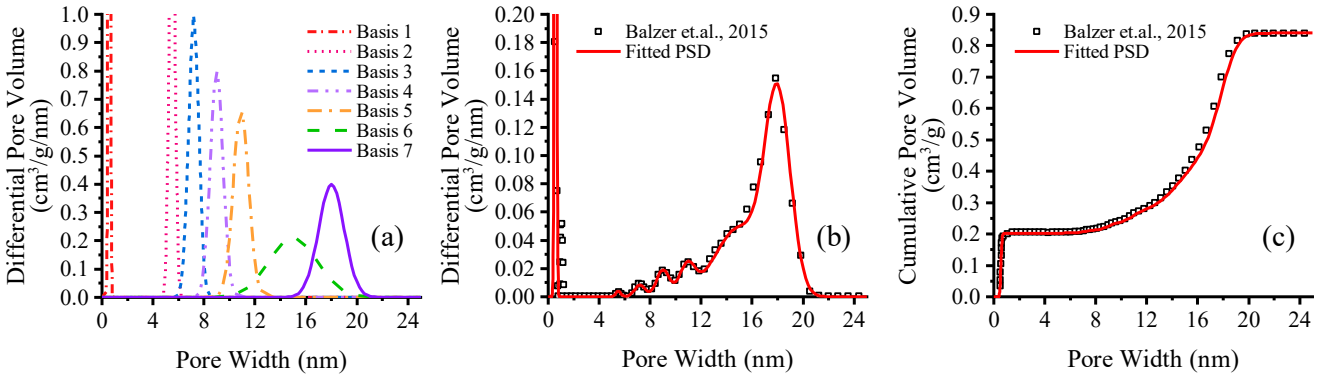

Fig. 6. Continuous representation of the PSD data: (a) basis functions, (b) summation of weighted basis functions to match the differential PSD, and (c) cumulative PSD match.

Table 1. Basis function parameters used in matching PSD in Fig. 6

Basis	Peak,	*w*	Weight
1	0.57	0.07	0.2397
2	5.50	0.20	0.0025
3	7.20	0.40	0.0102
4	9.00	0.50	0.0280
5	10.90	0.60	0.0362
6	15.00	1.90	0.2754
7	18.00	1.00	0.4080

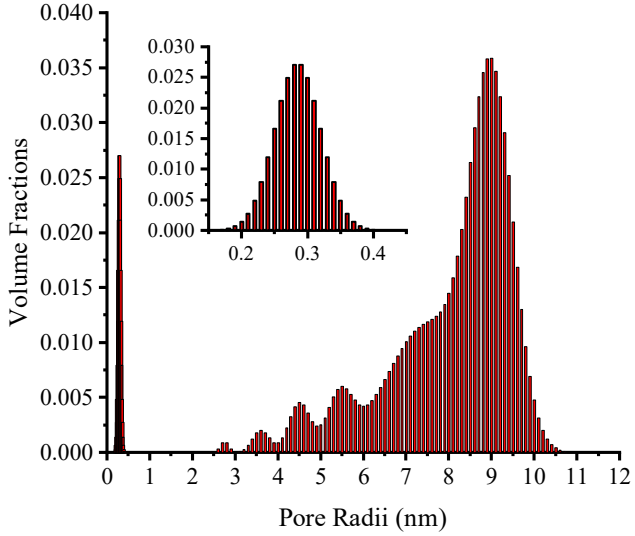

Fig. 7. Volume fractions of pore size bins corresponding to the porous carbon in Balzer et al. (2015).

Parameter calibration and model predictions

From the total pore volume per grams of sample ($0.86\,\mathrm{cm^3/g}$) and the mass density of the sample ($0.741\,\mathrm{g/cm^3}$) the initial porosity of the sample $\phi_0 = 0.637$ is deduced. The specific gravity of the solid $G_s = 1.45$ can be deduced from the particle density $\rho_s = 1.45$ g/cm^3. A microporous carbon rod sample with similar porosity has been reported by Balzer et al. (2011) with Young's modulus of about 7.24 GPa. Assuming $\nu = 0.1$, the bulk and shear moduli are calculated as $K = 3$ GPa and $G = 3.27$ GPa. The Biot's parameters are chosen as $b = 0.9$ and $N = 10$ GPa which are within the common ranges for porous carbon (Pijaudier-Cabot et al., 2011; Vandamme et al., 2010). The molar volume of nitrogen is $V_m = 34$ cm^3/mol. At $T \approx 77$ K, its additional adsorption heat is $Q = 440$ cal (Brunauer et al., 1940) and its saturation pressure is $p_0 = 97.2$ kPa (Lemmon, 1998). In addition to this general many-pore model, a mono-pore and a dual-pore model are also implemented to represent the PSD with one single pore size and two pore sizes, respectively. This is to examine whether the simplistic representation of the pore network as commonly done in the past (Eskandari-Ghadi and Zhang, 2021; Vandamme et al., 2010; Zhang, 2018) can yield similar result compared to the full PSD representation. The pore radii in the dual-pore model are chosen to represent the micropore (0.288 nm) and mesopore (9 nm) networks, respectively. The pore radius in the mono-pore model (1.13 nm) is chosen to give the same pore surface as the dual-pore model with the same porosity. Knowing that $\alpha = 2/3$ for spherical pores and K, ν, b, N, Q, V_m, p_0, T, and ϕ_0 are now constrained, parameters ΔE, C_h, and Γ_0 are adjusted for each PSD presentation to match the strain isotherm from Balzer et al. (2015). The full parameters are summarized in Table 2.

Predictions from the simplified mono-pore, the dual-pore, and the full PSD models are shown in Fig. 8. It is observed that the adsorption-induced deformation including the initial contraction can be accurately captured by either model. This is not surprising as the parameters are calibrated for the strain isotherm. Upgrading from single-pore to dual-pore representation shows significant enhancement in the predicted adsorption isotherm. Specifically, the addition of mesopores (9 nm) in the dual-pore model permits more space for adsorption to continue (Fig. 8b) after the micropore capacity quickly exhausted at low pressures (Fig. 8a). Comparing Figs. 8b and 8c shows drastic improvement of the predicted shape of the adsorption isotherm across low- and high- pressure regimes after incorporation of the full PSD. It is worth to note that the progressive enhancement of the agreement in the three figures is achieved by

using the same poroelasticity parameters with only slight adjustments on a few adsorption parameters (underlined in Table 2). All parameters are still within their realistic ranges. The fact that the same model yields better accuracy as the PSD input gains accuracy suggests that the underlying physics of adsorption straining is successfully captured by our theory. This permits one to investigate the sensitivity of the adsorption-deformation responses to the PSD of the porous material.

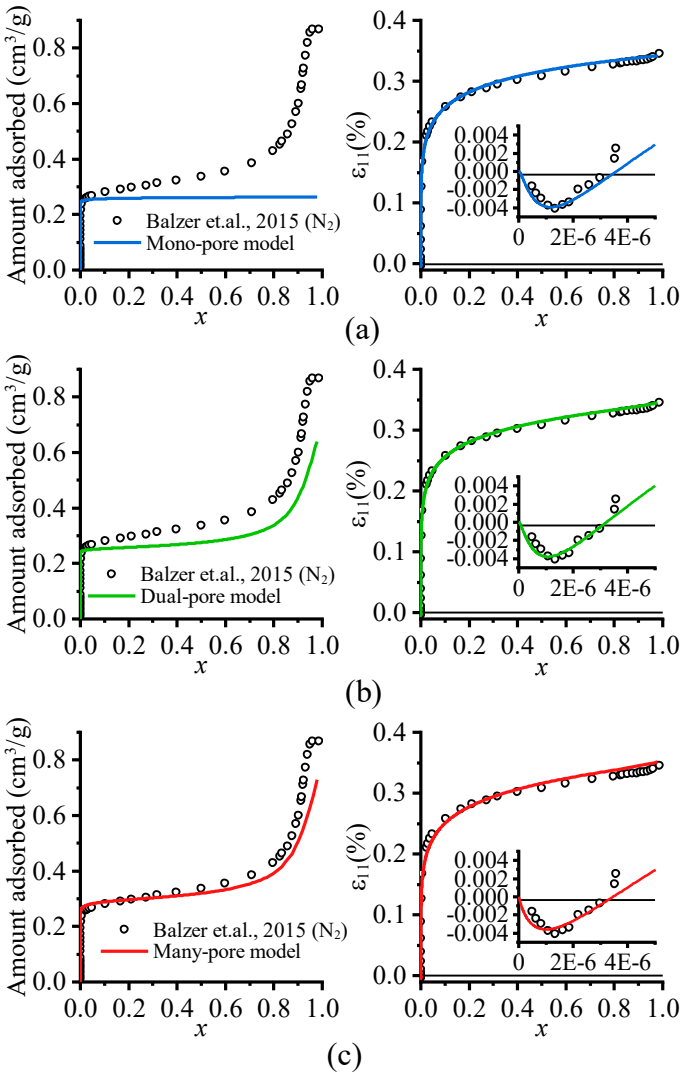

Fig. 8. Performance of the (a) mono-pore, (b) dual-pore, and (c) many-pore (using the exact PSD in Fig. 7) models and the progressive improvement as PSD input gains resolution.

Table 2. Parameters for the mono, dual, and many-pore models for the carbon – N_2 system of Balzer et al. (2015)

Parameter	Unit	Values		
		Mono-pore	Dual-pore	Many-pore
Poroelasticity				
K	[GPa]	3.0	3.0	3.0
G	[GPa]	3.27	3.27	3.27
b	[-]	0.9	0.9	0.9
N	[GPa]	10	10	10
Adsorption				
ΔE	[cal]	2090	2090	1940
Q	[cal]	440	440	440
C_h	[1/nm]	1.656	6.452	7.143
Γ_0	[μmol/m^2]	1.905	1.905	1.950
Microstructure				
ϕ_0	[-]	0.64	0.64	0.64
α	[-]	0.667	0.667	0.667
$R_{1,0}$	[nm]	1.13	0.288	PVD in Fig. 7
$R_{2,0}$	[nm]	-	9	
r_1	[-]	1.00	0.23	
r_2	[-]	-	0.77	

6 EFFECTS OF PSD ON THE SORPTIVE BEHAVIOR OF POROUS MATERIALS

All studies in this section take the same material properties from the previous section (many-pore model in Table 2) with merely the PSD input altered.

Effect of peak pore size

The first study examines the effect of shifting peak from smaller micropores towards larger micropores with the same shape of the PSD. Using Eq. (52), four differential PSDs with width $w = 0.1$ and peak radii of 0.285 nm, 0.300 nm, 0.315 nm, and 0.330 nm are generated. They are presented in Fig. 9a and their corresponding adsorption and strain isotherms are presented in Fig. 9b. It is observed that a slight shift in PSD towards mesopores can drastically diminish the initial contraction. This is consistent with the observation in Fig. 5b that large attractive disjoining pressure only presents for small pores at low pressure level. The adsorption isotherm on the other hand is hardly affected by such small change in the PSD. It is also noted that the PSD shifting does not affect much the swelling responses, i.e., a 16%

increase in microporous peak pore size (from 0.285nm to 0.330nm) only cause the maximum swelling strain decreases less than 8%.

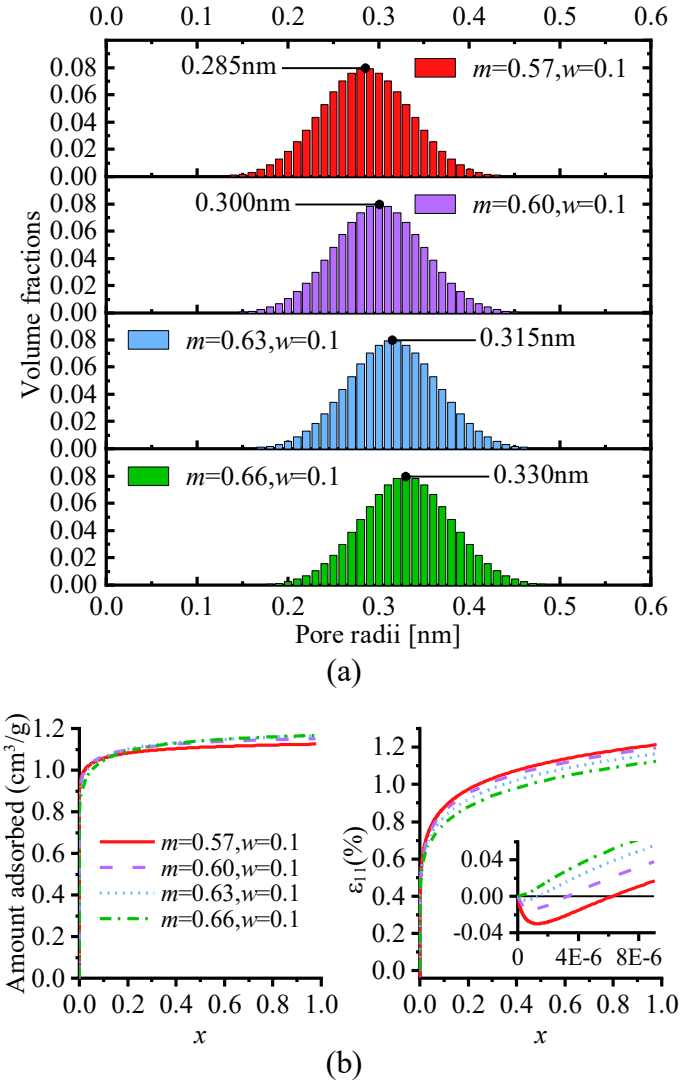

Fig. 9. Prediction of microporous carbon response to nitrogen adsorption with: (a) shifts of pore size distribution in microporous range; (b) amounts adsorbed and axial deformation.

Now, the same PSDs are shifted to the mesoporous range (Fig. 10a) with the predicted responses presented in Fig. 10b. Pure Bangham's expansion with no initial contraction (i.e., type-II strain isotherm) is predicted for this range of pore sizes. This is expected because of the diminished disjoining pressure for mesopores (Fig. 5b). The overall swelling of mesoporous material is predicted to be one order of magnitude less than that of microporous materials. This is because, for the same porosity, larger pores provide less surface area available to adsorption, thus weakening the swelling effects associated with the reduction of surface tension. It is worth to note that the commonly observed contraction at

intermediate pressures (Chen, 2019) is not captured by the model. This is because the underlying physics namely the formation of concave menisci through capillary condensation has not been implemented in our pore-scale model yet. This non-trivial task shall be pursued in follow-up studies.

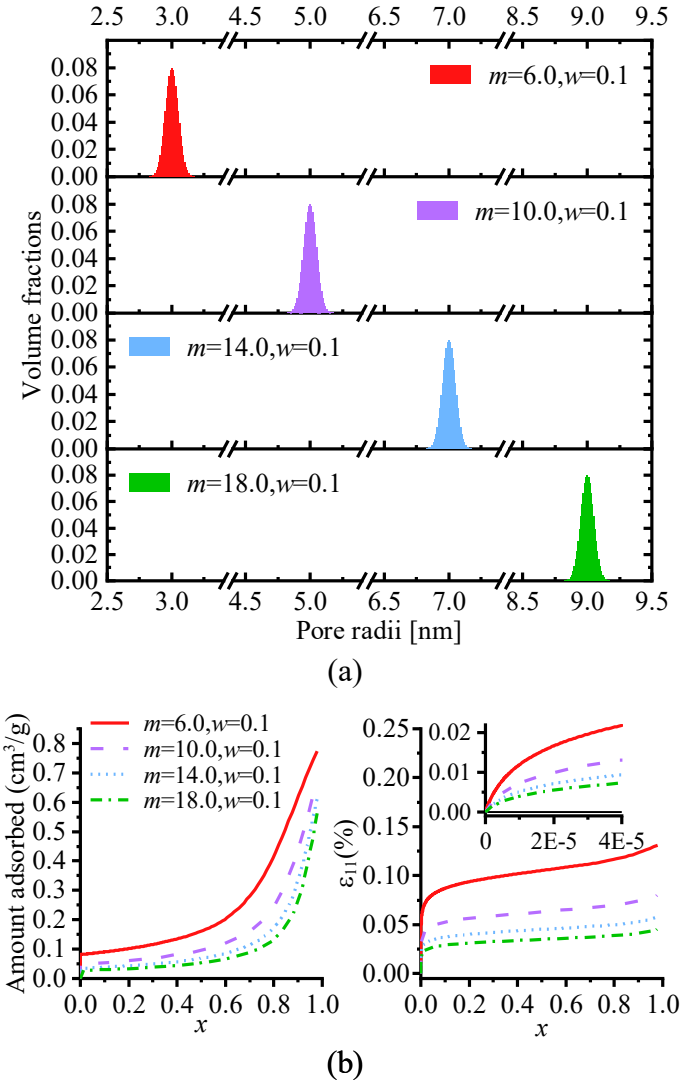

Fig. 10. Prediction of mesoporous carbon response to nitrogen adsorption with: (a) shifts of pore size distribution in mesoporous range; (b) amounts adsorbed and axial deformation.

As expected, the total amount of adsorption continues to decrease for distributions with larger pore sizes. For both microporous and mesoporous material, the model predicts that adsorption develops at a rapid rate initially, presumably as the first layer of adsorbates are attracted to the pore walls. Such rapid rate consistently diminishes at partial pressure of $x \approx 10^{-5}$, implying that the rate at which the first layer is filled is not affected by the pore size, in a manner similar to free-surface adsorption. At increased pressures, the very first few layers of adsorbates rapidly fill up the micropores, thus the system's

maximum adsorption capacity is quickly reached. On the other hand, mesopores can accommodate many layers of adsorbate, therefore the amount of adsorption keep increase at a slower rate after the initial filling of the first layer. The adsorption speeds up upon complete filling of all mesopores near the saturation pressure.

To summarize, under fixed total porosity and width of the PSD, smaller pores provide more surface area for adsorption and narrower wall separation. This has three effects: (1) rapid filling of the pore at the beginning of adsorption; (2) amplified swelling strain at high-pressure regime due to the Bangham's effect; (3) possible contraction strain at low-pressure regime due to the attractive disjoining pressure in micropores.

Effect of pore size dispersity

This section studies the effect of the PSD width on the adsorption-deformation characteristics. In the first set, a series of PSDs in the microporous range are gradually skewed towards the mesoporous range, using the logarithmic-normal distribution:

$$P(D/D_0) = \frac{1}{D/D_0 \cdot w\sqrt{2\pi}} e^{-\frac{1}{2}\left(\frac{\ln(D/D_0)-m}{w}\right)^2} \tag{53}$$

Similar to Eq. (52), $D_0 = 1$ nm is a normalization parameter and w controls both the width and skewness of the distribution. Unlike the normal distribution, the peak pore width is no longer $D_0 m$ but instead given by $\mathbb{M} = D_0 \exp(m - w^2)$. The mean of the log-normal distribution is given by $D_0 \exp(m + w^2/2)$. Here we start with a narrow PSD with peak pore radius of $R_{peak} = \mathbb{M}/2 = 0.25$nm and $w = 0.2$, then generated other PSDs by dispersing it towards the mesoporous range (increasing w) while maintaining constant R_{peak}.

The input PSDs and the predicted material responses are presented in Fig. 11. The first observation is that both the adsorption and the strain isotherms vary drastically, despite that the peak pore sizes are the same for all four simulations. This is true even for the first two PSDs ($w = 0.1$ and $w = 0.3$) where all pores are within the microporous range (<2 nm in width). Fig. 11b suggest that contraction diminishes as the material incorporates more mesopores and less micropores. This is in agreement with recent studies (Chen, 2019) that adsorption behavior of type I is observed for microporous material which

transforms into adsorption behavior of type III as meso/macro pores are added to the system. However, even with 67.3% of total pore volume in the mesoporous range and only 32.7% in the microporous range, slight initial contraction can still be observed.

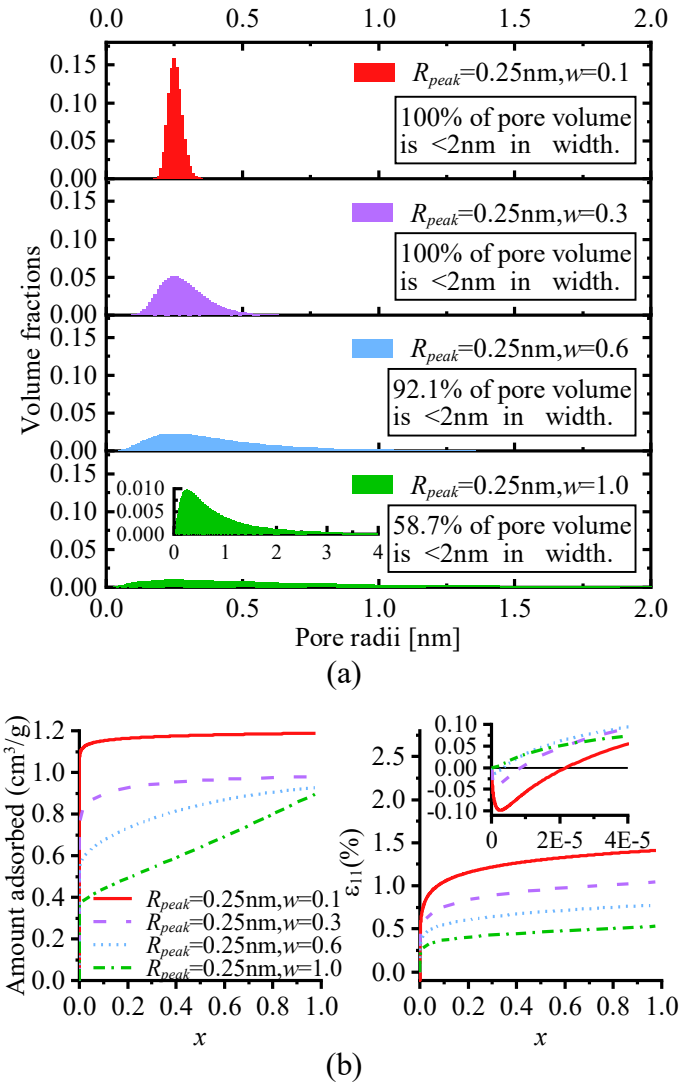

Fig. 11. Prediction of microporous carbon response to nitrogen adsorption with: (a) dispersion of micro pore sizes towards meso por sizes with same peak pore size; (b) amounts adsorbed and axial deformation.

This suggests that the material's IUPAC classification (i.e., micro/meso porous) cannot fully disclose whether it will exhibit initial contraction upon adsorption. Based on the proposed theory, how the material behaves is closely related to whether the adsorbed surfaces overlap or not (Fig. 2b), which strongly depends on the type of adsorbent-adsorbate interactions and the size of the adsorbate molecules. Several features observed earlier are again highlighted in Fig. 11b: adsorption quickly reaches maximum capacity at low pressures for microporous material while it becomes more gradual after the initial filling

for mesoporous solids. More mesopores reduces the surfaces available for adsorption, thus reducing the total adsorption capacity and the induced swelling.

In the second set, four PSDs in the mesopore range are generated using the normal distributions (Eq. (52)) with fixed peak pore radius of 4nm and different widths using $w = 0.2 \sim 3.125$. The PSDs are presented in Fig. 12a and the model predictions are presented in Fig. 12b. The intriguingly simple results suggest that for PSDs in the mesoporous range, the narrowness of the PSD has little effect on the material response.

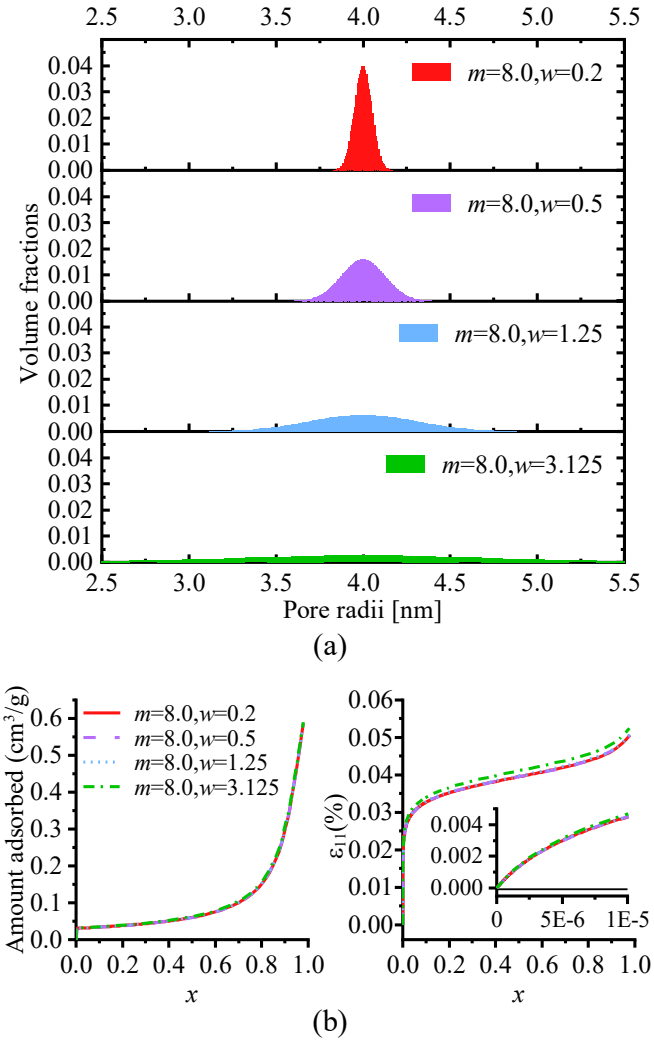

Fig. 12. Prediction of mesoporous carbon response to nitrogen adsorption with: (a) diffusion of pore size distribution in mesoporous range; (b) amounts adsorbed and axial deformation.

This is a quite convenient conclusion as the information of peak pore size is sufficient in determining the adsorption-deformation response of pure mesoporous materials. It is thus reassuring that poromechanical

theories that rely on single pore size descriptors such as in Zhang (2018) can be still accurate in describing mesoporous solids. Combining the results in Fig. 11 and Fig. 12, one may deduce that as the pore size becomes larger, the actual distribution of pore sizes loses significance and information of the peak pore size becomes sufficient.

To summarize, the results presented in Figures 9 to 12 indicate that: (1) micropores are main cause of initial contraction; and (2) a fine resolution of the PSD in the microporous range is necessary for accurate prediction of the material response, while a coarse resolution and even a single peak pore size may be sufficient for modeling mesoporous materials.

Relation between PSD and initial contraction

The above analyses show that the initial contraction is affected by both the peak pore size and the width of the PSD. It is possible to quantify such dependency by plotting the maximum contraction strain with respect to peak pore radius R_{peak} at different w values, as shown in Fig. 13. All simulations use the same parameters as in Table 2 for the many-pore model. Fig. 13a shows that all curves share the same trend that contraction first intensifies and then gradually reduces to zero as the peak pore size increases. It is also observed that as the PSD becomes narrower, e.g., the case of $w = 0.05$, the increase in initial contraction with increasing R_{peak} becomes sharper and the maximum contraction becomes stronger. The curves for wider PSDs in Fig. 13a are more dispersed simply because not all pores enter and exit the contractive range simultaneously.

A closer inspection of Fig. 13a suggests that even when the pore width is smaller than the size of one adsorbate molecule (i.e., $R < R_0 = 0.21$ nm for the selected parameters in Table 2), some amount of adsorption and strain are still predicted by the model. This is because the BDDT model Eq. (51) is continuous and gives non-zero adsorption even when the number of adsorbed layers ($n = C_h h$) is less than 1. To enforce a physical lower bound below which the pores are inaccessible to adsorbates, a crude way is to implement a hard cutoff on the BDDT isotherm such that $\Gamma = 0$ when $n < 1$. The predicted contraction strains after enforcing such cutoff are presented in Fig. 13b. It is observed that narrower the PSD results in more abrupt maximum contraction curve around the cut-off size $R_0 = 0.21$ nm. Below this value, no adsorption is possible and thus adsorption-induced strain is nearly zero. Comparing Fig. 13a and b indicates that the upper bound of the contraction range is not affected by such cut-off, and the overall size of contraction regime is reduced. This implies that some microporous network may not

exhibit initial contraction at all when interacting with large adsorbate molecules. Finally, it is interesting to note that the adsorbate radius $R_0 = 0.21$ nm or diameter 0.42 nm deduced from model calibration is very close to the kinetic diameter of the nitrogen molecule, 0.364 nm (Ismail et al., 2015).

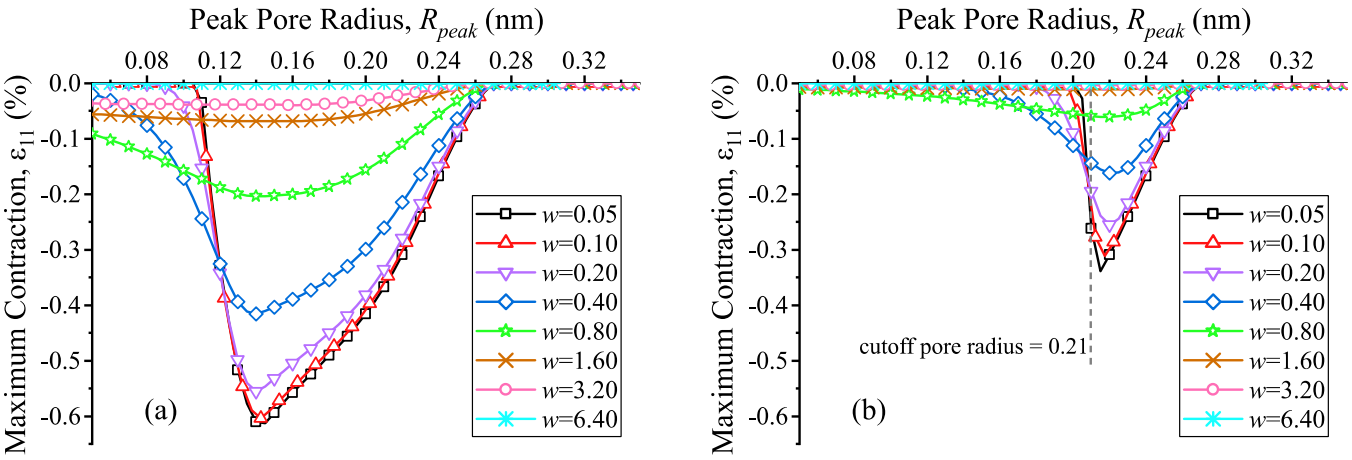

Fig. 13. Maximum initial contraction in variation with peak pore radius for different PSD skewness for (a) the current theory, and (b) the current theory with BDDT adsorption model cut off for $n < 1$. Each point along each curve corresponds to a PSD generated by Eq. (53) using $D_0 = 1\text{nm}$, $R_{peak} = 0.1\text{nm}$, and the corresponding w. Then the PSD is shifted along the pore size axis to obtain PSDs of the same shape with different peak pore radii. The remaining model input parameters are taken the same as the many-pore model in Table 2.

7 CONCLUSION

We developed a framework to incorporate the surface tension and disjoining pressure effects for adsorptive porous materials with generic pore size distributions. Specifically, we constructed the total surface free energy of a general pore network by statistically homogenizing the free energy of many equivalent slit pores. Then the decomposition of the total material dissipation into the solid, fluid, and surface contributions leads to the free energy balance equations of the three phases of the REV. The incremental form of a general poroelastic relation is then derived from the solid free energy balance to gain versatility in both implementation and modification of the framework. To validate the proposed theory, a constitutive model is constructed by specifying isotropic linear poroelasticity, the BDDT adsorption model, spherical pore structure, and a linear mapping of pore radii to slit-pore width. By choosing physical values for the material parameters and inputting the measured pore size distribution (PSD), the model performance is validated against the experimental data on nitrogen adsorption on porous carbons (Balzer et al., 2015). The model that takes the information of the full PSD shows significantly better agreements with experimental data in comparison to the single-pore and dual-pore representations of the same PSD. Using the same set of parameters, the effect of PSD on the predicted

adsorption and strain isotherms are investigated through a systematic parametric study, the main conclusions of which are highlighted below:

1. Inclusion of surface tension and disjoining pressure in the poromechanical theory can explain the transition from initial contraction to overall swelling of microporous materials upon adsorption. Specifically, in absence of stretch-dependent surface stress, the initial contraction is caused by the presence of attractive disjoining pressure which is most prominent when the pore sizes gather closely around the size of only a few adsorbate molecules. For meso/macro porous materials where disjoining pressure vanishes, sorption-induced deformation is governed by the reduction of surface tension which indicates swelling.

2. In terms of adsorption isotherms, microporous material shows rapid filling of pore spaces at very low pressures. The inclusion of mesopores permits more space for adsorption to continue at higher pressure levels.

3. PSD is important for microporous materials because slight shifting in peak pore size and dispersity affects the predicted strain isotherms. For mesoporous materials, the full information of PSD loses significance and only the peak pore size matters in predicting their adsorption-deformation responses. This is convenient in that poromechanical theories that rely on single pore size descriptors can be still quite accurate for mesoporous solids.

Within the presented framework, further improvements can be contemplated by (1) introducing capillary condensation in pore-scale models to capture the contraction of porous materials at intermediate pressure levels; (2) introducing the two-way adsorption-deformation coupling by making both PSD and surface tension dependent on skeleton deformation; (3) incorporating finite-strain poroelastic models. Some fundamental aspects need to be further studied, including the mechanics behind the sorption-deformation hysteresis and the surface forces in pores of different shapes.

8 DECLARATION OF COMPETING INTEREST

The authors declare that they have no known competing financial interests or personal relationships that could have appeared to influence the work reported in this paper.

9 ACKNOWLEDGEMENT

This research was supported by the U.S. National Science Foundation (NSF) under NSF CMMI Award No. 2113474.

10 REFERENCES

Amberg, C., McIntosh, R., 1952. A study of adsorption hysteresis by means of length changes of a rod of porous glass. Canadian Journal of Chemistry 30, 1012-1032.

Ash, S.G., Everett, D.H., Radke, C., 1973. Thermodynamics of the effects of adsorption on interparticle forces. Journal of the Chemical Society, Faraday Transactions 2 69, 1256.

Baek, S., Pence, T.J., 2009. On swelling induced degradation of fiber reinforced polymers. International Journal of Engineering Science 47, 1100-1109.

Balbuena, P.B., Berry, D., Gubbins, K.E., 1993. Solvation pressures for simple fluids in micropores. The Journal of Physical Chemistry 97, 937-943.

Balzer, C., Braxmeier, S., Neimark, A.V., Reichenauer, G., 2015. Deformation of Microporous Carbon during Adsorption of Nitrogen, Argon, Carbon Dioxide, and Water Studied by in Situ Dilatometry. Langmuir : the ACS journal of surfaces and colloids 31, 12512–12519.

Balzer, C., Wildhage, T., Braxmeier, S., Reichenauer, G., Olivier, J.P., 2011. Deformation of porous carbons upon adsorption. Langmuir : the ACS journal of surfaces and colloids 27, 2553–2560.

Bangham, D., Fakhoury, N., 1928. The expansion of charcoal accompanying sorption of gases and vapours. Nature 122, 681.

Biot, M.A., 1941. General theory of three‐dimensional consolidation. Journal of applied physics 12, 155-164.

Brochard, L., Vandamme, M., Pellenq, R.J.-M., 2012a. Poromechanics of microporous media. Journal of the Mechanics and Physics of Solids 60, 606–622.

Brochard, L., Vandamme, M., Pellenq, R.J.-M., Fen-Chong, T., 2012b. Adsorption-induced deformation of microporous materials: coal swelling induced by CO2-CH4 competitive adsorption. Langmuir : the ACS journal of surfaces and colloids 28, 2659–2670.

Brunauer, S., Deming, L.S., Deming, W.E., Teller, E., 1940. On a Theory of the van der Waals Adsorption of Gases. Journal of the American Chemical Society 62, 1723–1732.

Brunauer, S., Emmett, P.H., Teller, E., 1938. Adsorption of Gases in Multimolecular Layers. Journal of the American Chemical Society 60, 309–319.

Champeau, M., Thomassin, J.-M., Jérôme, C., Tassaing, T., 2014. In situ FTIR micro-spectroscopy to investigate polymeric fibers under supercritical carbon dioxide: CO2 sorption and swelling measurements. The Journal of Supercritical Fluids 90, 44-52.

Chen, M., 2019. Sorption-Induced Deformation of Nanoporous Materials. ETH Zurich.

Chen, M., Coasne, B., Guyer, R., Derome, D., Carmeliet, J., 2018. Role of hydrogen bonding in hysteresis observed in sorption-induced swelling of soft nanoporous polymers. Nature communications 9, 1-7.

Chen, M., Coasne, B., Guyer, R., Derome, D., Carmeliet, J., 2019. Molecular simulation of sorption-induced deformation in atomistic nanoporous materials. Langmuir 35, 7751-7758.

Chen, M., Coasne, B., Guyer, R., Derome, D., Carmeliet, J., 2020. A Poromechanical Model for Sorption Hysteresis in Nanoporous Polymers. The Journal of Physical Chemistry B 124, 8690-8703.

Colina, H., Roux, S., 2000. Experimental model of cracking induced by drying shrinkage. The European Physical Journal E 1, 189-194.

Coudert, F.-X., Boutin, A., Fuchs, A.H., Neimark, A.V., 2013. Adsorption Deformation and Structural Transitions in Metal–Organic Frameworks: From the Unit Cell to the Crystal. The Journal of Physical Chemistry Letters 4, 3198–3205.

Coussy, O., 2004. Poromechanics. John Wiley & Sons.

Coussy, O., 2010. Mechanics and physics of porous solids. John Wiley & Sons.

Dawson, C., Vincent, J.F., Rocca, A.-M., 1997. How pine cones open. Nature 390, 668-668.

de Feijter, J., 1988. Thin Liquid Films.: 1. Thermodynamics of thin liquid films, in: Ivanov, I. (Ed.). CRC Press.
DeHoff, R., 2006. Thermodynamics in materials science. CRC Press.
Dolino, G., Bellet, D., Faivre, C., 1996. Adsorption strains in porous silicon. Physical Review B 54, 17919.
El Tabbal, G., Dangla, P., Vandamme, M., Bottoni, M., Granet, S., 2020. Modelling the drying shrinkage of porous materials by considering both capillary and adsorption effects. Journal of the Mechanics and Physics of Solids, 104016.
Elbaum, R., Zaltzman, L., Burgert, I., Fratzl, P., 2007. The role of wheat awns in the seed dispersal unit. Science 316, 884-886.
Eskandari-Ghadi, M., Zhang, Y., 2021. Mechanics of shrinkage-swelling transition of microporous materials at the initial stage of adsorption. International Journal of Solids and Structures 222, 111041.
Everett, D., 1972. Manual of symbols and terminology for physicochemical quantities and units, appendix II: Definitions, terminology and symbols in colloid and surface chemistry. Pure and Applied Chemistry 31, 577-638.
Fomkin, A., 2005. Adsorption of gases, vapors and liquids by microporous adsorbents. Adsorption 11, 425-436.
Gor, G.Y., Bernstein, N., 2016. Revisiting Bangham's law of adsorption-induced deformation: changes of surface energy and surface stress. Physical chemistry chemical physics : PCCP 18, 9788–9798.
Gor, G.Y., Huber, P., Bernstein, N., 2017. Adsorption-induced deformation of nanoporous materials—A review. Applied Physics Reviews 4, 011303.
Grégoire, D., Malheiro, C., Miqueu, C., 2018. Estimation of adsorption-induced pore pressure and confinement in a nanoscopic slit pore by a density functional theory. Continuum Mechanics and Thermodynamics 30, 347-363.
Haines, R.S., McIntosh, R., 1947. Length Changes of Activated Carbon Rods Caused by Adsorption of Vapors. Journal of the American Chemical Society 15, 28–38.
Hansen, W., 1987. Drying shrinkage mechanisms in Portland cement paste. Journal of the American Ceramic society 70, 323-328.
Heller, R., Zoback, M., 2014. Adsorption of methane and carbon dioxide on gas shale and pure mineral samples. Journal of unconventional oil and gas resources 8, 14-24.
Ismail, A.F., Khulbe, K.C., Matsuura, T., 2015. Gas separation membranes. Switz. Springer 10, 978-973.
Israelachvili, J.N., 2011. Intermolecular and surface forces. Academic press.
Kowalczyk, P., Ciach, A., Neimark, A.V., 2008. Adsorption-induced deformation of microporous carbons: pore size distribution effect. Langmuir : the ACS journal of surfaces and colloids 24, 6603–6608.
Kowalczyk, P., Furmaniak, S., Gauden, P.A., Terzyk, A.P., 2012. Methane-induced deformation of porous carbons: From normal to high-pressure operating conditions. The Journal of Physical Chemistry C 116, 1740-1747.
Kramer, D., Weissmüller, J., 2007. A note on surface stress and surface tension and their interrelation via Shuttleworth's equation and the Lippmann equation. Surface Science 601, 3042-3051.
Lakhanpal, M.L., Flood, E.A., 1957. Stresses and strains in adsorbate–adsorbent systems: Iv. Contractions of activated carbon on adsorption of gases and vapors at low initial pressures. Canadian Journal of Chemistry 35, 887–899.
Langmuir, I., 1918. The adsorption of gases on plane surfaces of glass, mica and platinum. Journal of the American Chemical Society 40, 1361–1403.
Lee, Y., Kim, S.K., Park, Y.J., Cho, J., Koo, H.J., 2019. A humidity‐sensing composite microfiber based on moisture‐induced swelling of an agarose polymer matrix. Polymer Composites 40, 3582-3587.
Lemmon, E.W., 1998. Thermophysical properties of fluid systems. NIST chemistry WebBook.

Levine, J.R., 1996. Model study of the influence of matrix shrinkage on absolute permeability of coal bed reservoirs. Geological Society, London, Special Publications 109, 197-212.
Lyu, Q., Ranjith, P., Long, X., Kang, Y., Huang, M., 2015. A review of shale swelling by water adsorption. Journal of Natural Gas Science and Engineering 27, 1421-1431.
Meehan, F.T., 1927. The Expansion of Charcoal on Sorption of Carbon Dioxide. Proceedings of the Royal Society A: Mathematical, Physical and Engineering Sciences 115, 199–207.
Pijaudier-Cabot, G., Vermorel, R., Miqueu, C., Mendiboure, B., 2011. Revisiting poromechanics in the context of microporous materials. Comptes Rendus Mécanique 339, 770–778.
Rahaman, A., Grassian, V.H., Margulis, C.J., 2008. Dynamics of water adsorption onto a calcite surface as a function of relative humidity. The Journal of Physical Chemistry C 112, 2109-2115.
Ravikovitch, P.I., Neimark, A.V., 2006. Density functional theory model of adsorption deformation. Langmuir 22, 10864-10868.
Reichenauer, G., Scherer, G., 2001. Nitrogen sorption in aerogels. Journal of non-crystalline solids 285, 167-174.
Rey, J., Vandamme, M., 2013. On the shrinkage and stiffening of a cellulose sponge upon drying. Journal of Applied Mechanics 80.
Rusanov, A.I., 1966. Thermodynamics of films. 2. Equilibrium conditions and elasticity of flat thin films. COLLOID JOURNAL-USSR 28, 583–588.
Serre, C., Mellot-Draznieks, C., Surblé, S., Audebrand, N., Filinchuk, Y., Férey, G., 2007. Role of solvent-host interactions that lead to very large swelling of hybrid frameworks. Science 315, 1828-1831.
Setzer, M., Wittmann, F., 1974. Surface energy and mechanical behaviour of hardened cement paste. Applied physics 3, 403-409.
Van Opdenbosch, D., Fritz‐Popovski, G., Wagermaier, W., Paris, O., Zollfrank, C., 2016. Moisture‐Driven Ceramic Bilayer Actuators from a Biotemplating Approach. Advanced Materials 28, 5235-5240.
Vandamme, M., 2019. Coupling between adsorption and mechanics (and vice versa). Current Opinion in Chemical Engineering 24, 12–18.
Vandamme, M., Brochard, L., Lecampion, B., Coussy, O., 2010. Adsorption and strain: The CO2-induced swelling of coal. Journal of the Mechanics and Physics of Solids 58, 1489–1505.
Wiig, E.O., Juhola, A., 1949. The adsorption of water vapor on activated charcoal. Journal of the American Chemical Society 71, 561-568.
Yang, X., Wang, W., Miao, M., 2018. Moisture-responsive natural fiber coil-structured artificial muscles. ACS applied materials & interfaces 10, 32256-32264.
Zhang, Y., 2018. Mechanics of adsorption–deformation coupling in porous media. Journal of the Mechanics and Physics of Solids 114, 31–54.
Zhao, Q., Dunlop, J.W., Qiu, X., Huang, F., Zhang, Z., Heyda, J., Dzubiella, J., Antonietti, M., Yuan, J., 2014. An instant multi-responsive porous polymer actuator driven by solvent molecule sorption. Nature communications 5, 4293.

APPENDIX A. INCREMENTAL CONSTITUTIVE RELATIONS IN EXPLICIT FORM

The first step towards the explicit form of Eq. (25) is to expand $d\overline{\Pi}$, $d\left(\overline{\gamma}_p \partial A_s / \partial \varepsilon_{ij}\right)$, and $d\left(\overline{\gamma}_p \partial A_s / \partial \phi\right)$ considering the definition of smeared surface forces Eqs. (13):

$$d\overline{\Pi} = \frac{\partial \overline{\Pi}}{\partial p} dp + \frac{\partial \overline{\Pi}}{\partial \phi} d\phi + \frac{\partial \overline{\Pi}}{\partial \varepsilon_{kl}} d\varepsilon_{kl} \tag{54}$$

$$\begin{aligned} d\left(\frac{\partial A_s}{\partial \varepsilon_{ij}} \sum \frac{\partial \mathcal{A}_K}{\partial \mathcal{A}} \gamma_{p,K} \right) = & \frac{\partial A_s}{\partial \varepsilon_{ij}} \frac{\partial \overline{\gamma}_p}{\partial p} dp + \frac{\partial A_s}{\partial \varepsilon_{ij}} \frac{\partial \overline{\gamma}_p}{\partial \phi} d\phi + \frac{\partial A_s}{\partial \varepsilon_{ij}} \frac{\partial \overline{\gamma}_p}{\partial \varepsilon_{kl}} d\varepsilon_{kl} \\ & + \frac{\partial^2 A_s}{\partial \phi \partial \varepsilon_{ij}} \overline{\gamma}_p d\phi + \frac{\partial^2 A_s}{\partial \varepsilon_{kl} \partial \varepsilon_{ij}} \overline{\gamma}_p d\varepsilon_{kl} \end{aligned} \tag{55}$$

$$\begin{aligned} d\left(\frac{\partial A_s}{\partial \phi} \overline{\gamma}_p \right) = & \frac{\partial A_s}{\partial \phi} \frac{\partial \overline{\gamma}_p}{\partial p} dp + \frac{\partial A_s}{\partial \phi} \frac{\partial \overline{\gamma}_p}{\partial \phi} d\phi + \frac{\partial A_s}{\partial \phi} \frac{\partial \overline{\gamma}_p}{\partial \varepsilon_{kl}} d\varepsilon_{kl} \\ & + \frac{\partial^2 A_s}{\partial \phi^2} \overline{\gamma}_p d\phi + \frac{\partial^2 A_s}{\partial \varepsilon_{kl} \partial \phi} \overline{\gamma}_p d\varepsilon_{kl} \end{aligned} \tag{56}$$

Substituting Eqs. (54)-(56) into Eq. (25) and reorganizing gives

$$\begin{aligned} d\sigma_{ij} = & \left(C^{\varepsilon}_{ijkl} + \frac{\partial A_s}{\partial \varepsilon_{ij}} \frac{\partial \overline{\gamma}_p}{\partial \varepsilon_{kl}} + \frac{\partial^2 A_s}{\partial \varepsilon_{kl} \partial \varepsilon_{ij}} \overline{\gamma}_p \right) d\varepsilon_{kl} + \left(C^{\varepsilon\phi}_{ij} + \frac{\partial A_s}{\partial \varepsilon_{ij}} \frac{\partial \overline{\gamma}_p}{\partial \phi} + \frac{\partial^2 A_s}{\partial \phi \partial \varepsilon_{ij}} \overline{\gamma}_p \right) d\phi \\ & + \frac{\partial A_s}{\partial \varepsilon_{ij}} \sum \frac{\partial \mathcal{A}_K}{\partial \mathcal{A}} \frac{\partial \gamma_{p,K}}{\partial p} dp \end{aligned} \tag{57}$$

$$dp = \frac{C^{\varepsilon\phi}_{kl} + \frac{\partial A_s}{\partial \phi} \frac{\partial \overline{\gamma}_p}{\partial \varepsilon_{kl}} + \frac{\partial^2 A_s}{\partial \varepsilon_{kl} \partial \phi} \overline{\gamma}_p - \frac{\partial \overline{\Pi}}{\partial \varepsilon_{kl}}}{1 - \frac{\partial A_s}{\partial \phi} \frac{\partial \overline{\gamma}_p}{\partial p} - \frac{\partial \overline{\Pi}}{\partial p}} d\varepsilon_{kl} + \frac{C^{\phi} + \frac{\partial A_s}{\partial \phi} \frac{\partial \overline{\gamma}_p}{\partial \phi} + \frac{\partial^2 A_s}{\partial \phi^2} \overline{\gamma}_p - \frac{\partial \overline{\Pi}}{\partial \phi}}{1 - \frac{\partial A_s}{\partial \phi} \frac{\partial \overline{\gamma}_p}{\partial p} - \frac{\partial \overline{\Pi}}{\partial p}} d\phi \tag{58}$$

Substitution of Eq. (58) into Eq. (57) yields

$$\begin{aligned} d\sigma_{ij} = & \left(C^{\varepsilon}_{ijkl} + \frac{\partial A_s}{\partial \varepsilon_{ij}} \frac{\partial \overline{\gamma}_p}{\partial \varepsilon_{kl}} + \frac{\partial^2 A_s}{\partial \varepsilon_{kl} \partial \varepsilon_{ij}} \overline{\gamma}_p \right) d\varepsilon_{kl} + \left(C^{\varepsilon\phi}_{ij} + \frac{\partial A_s}{\partial \varepsilon_{ij}} \frac{\partial \overline{\gamma}_p}{\partial \phi} + \frac{\partial^2 A_s}{\partial \phi \partial \varepsilon_{ij}} \overline{\gamma}_p \right) d\phi \\ & + \frac{1}{H} \frac{\partial A_s}{\partial \varepsilon_{ij}} \sum \frac{\partial \mathcal{A}_K}{\partial \mathcal{A}} \frac{\partial \gamma_{p,K}}{\partial p} \left(C^{\varepsilon\phi}_{kl} + C^{ads,p\varepsilon}_{kl} \right) d\varepsilon_{kl} + \frac{1}{H} \frac{\partial A_s}{\partial \varepsilon_{ij}} \sum \frac{\partial \mathcal{A}_K}{\partial \mathcal{A}} \frac{\partial \gamma_{p,K}}{\partial p} \left(C^{\phi} + C^{ads,p\phi} \right) d\phi \end{aligned} \tag{59}$$

Eqs. (59) and (58) are then simplified into Eqs. (26) and (27), respectively. The terms involving smeared quantities can be written as Eqs. (33)-(39) by invoking Eq. (13), the definitions $h_K = h_K(\boldsymbol{\varepsilon}, \phi)$ and $\mathcal{A}_K = \mathcal{A}_K(\boldsymbol{\varepsilon}, \phi)$, and the assumption that $\Omega_K^v / \Omega^v = r_K$ is constant.

APPENDIX B. DERIVATIVES OF SURFACE AREAS

The derivatives $\partial \mathcal{A}_K / \partial \mathcal{A}$, $\partial(\partial \mathcal{A}_K / \partial \mathcal{A}) / \partial \phi$, and $\partial(\partial \mathcal{A}_K / \partial \mathcal{A}) / \partial \varepsilon_{ij}$ can be derived by considering $\mathcal{A} = \mathcal{A}(\boldsymbol{\varepsilon}, \phi)$ and $\mathcal{A} = \sum \mathcal{A}_K$:

$$\frac{\partial \mathcal{A}_K}{\partial \mathcal{A}} = \frac{\partial \mathcal{A}_K}{\partial \phi}\frac{\partial \phi}{\partial \mathcal{A}} + \frac{\partial \mathcal{A}_K}{\partial \varepsilon_{ij}}\frac{\partial \varepsilon_{ij}}{\partial \mathcal{A}} = \frac{\partial\left(A_{s,K}\Omega_0\right)}{\partial \phi}\frac{\partial \phi}{\partial \sum A_{s,K}\Omega_0} + \frac{\partial\left(A_{s,K}\Omega_0\right)}{\partial \varepsilon_{ij}}\frac{\partial \varepsilon_{ij}}{\partial \sum A_{s,K}\Omega_0} \tag{60}$$

$$\begin{aligned}\frac{\partial}{\partial \phi}\frac{\partial \mathcal{A}_K}{\partial \mathcal{A}} &= \frac{\partial^2 \mathcal{A}_K}{\partial \phi^2}\frac{\partial \phi}{\partial \mathcal{A}} + \frac{\partial \mathcal{A}_K}{\partial \phi}\frac{\partial}{\partial \phi}\left(\frac{\partial \phi}{\partial \mathcal{A}}\right) + \frac{\partial^2 \mathcal{A}_K}{\partial \phi \partial \varepsilon_{ij}}\frac{\partial \varepsilon_{ij}}{\partial \mathcal{A}} + \frac{\partial \mathcal{A}_K}{\partial \varepsilon_{ij}}\frac{\partial}{\partial \phi}\left(\frac{\partial \varepsilon_{ij}}{\partial \mathcal{A}}\right) \\ &= \frac{\partial^2 \mathcal{A}_K}{\partial \phi^2}\frac{1}{\sum \frac{\partial \mathcal{A}_K}{\partial \phi}} - \frac{\partial \mathcal{A}_K}{\partial \phi}\frac{\sum \frac{\partial^2 \mathcal{A}_K}{\partial \phi^2}}{\left(\sum \frac{\partial \mathcal{A}_K}{\partial \phi}\right)^2} + \frac{\partial^2 \mathcal{A}_K}{\partial \phi \partial \varepsilon_{ij}}\frac{1}{\sum \frac{\partial \mathcal{A}_K}{\partial \varepsilon_{ij}}} + \frac{\partial \mathcal{A}_K}{\partial \varepsilon_{ij}}\frac{\sum \frac{\partial^2 \mathcal{A}_K}{\partial \phi \partial \varepsilon_{ij}}}{\sum \frac{\partial \mathcal{A}_K}{\partial \varepsilon_{kl}}\sum \frac{\partial \mathcal{A}_K}{\partial \varepsilon_{kl}}}\end{aligned} \tag{61}$$

$$\begin{aligned}\frac{\partial}{\partial \varepsilon_{ij}}\frac{\partial \mathcal{A}_K}{\partial \mathcal{A}} &= \frac{\partial^2 \mathcal{A}_K}{\partial \phi \partial \varepsilon_{ij}}\frac{\partial \phi}{\partial \mathcal{A}} + \frac{\partial \mathcal{A}_K}{\partial \phi}\frac{\partial}{\partial \varepsilon_{ij}}\left(\frac{\partial \phi}{\partial \mathcal{A}}\right) + \frac{\partial^2 \mathcal{A}_K}{\partial \varepsilon_{ij} \partial \varepsilon_{kl}}\frac{\partial \varepsilon_{kl}}{\partial \mathcal{A}} + \frac{\partial \mathcal{A}_K}{\partial \varepsilon_{kl}}\frac{\partial}{\partial \varepsilon_{ij}}\left(\frac{\partial \varepsilon_{kl}}{\partial \mathcal{A}}\right) \\ &= \frac{\partial^2 \mathcal{A}_K}{\partial \phi \partial \varepsilon_{ij}}\frac{1}{\sum \frac{\partial \mathcal{A}_K}{\partial \phi}} - \frac{\partial \mathcal{A}_K}{\partial \phi}\frac{\sum \frac{\partial^2 \mathcal{A}_K}{\partial \phi \partial \varepsilon_{ij}}}{\left(\sum \frac{\partial \mathcal{A}_K}{\partial \phi}\right)^2} + \frac{\partial^2 \mathcal{A}_K}{\partial \varepsilon_{ij} \partial \varepsilon_{kl}}\frac{1}{\sum \frac{\partial \mathcal{A}_K}{\partial \varepsilon_{kl}}} + \frac{\partial \mathcal{A}_K}{\partial \varepsilon_{kl}}\frac{\sum \frac{\partial^2 \mathcal{A}_K}{\partial \varepsilon_{ij} \partial \varepsilon_{kl}}}{\sum \frac{\partial \mathcal{A}_K}{\partial \varepsilon_{pq}}\sum \frac{\partial \mathcal{A}_K}{\partial \varepsilon_{pq}}}\end{aligned} \tag{62}$$

Eqs. (60)-(62) can be further simplified using $\mathcal{A}_K = A_{s,K}\Omega_0$ and $\mathcal{A} = \sum \mathcal{A}_K = A_s\Omega_0$, knowing that $A_{s,K}$ is generally a function of the kinematics, $\boldsymbol{\varepsilon}$ and ϕ:

$$\frac{\partial \mathcal{A}_K}{\partial \mathcal{A}} = \frac{\partial A_{s,K}}{\partial \phi}\frac{1}{\sum \frac{\partial A_{s,K}}{\partial \phi}} + \frac{\partial A_{s,K}}{\partial \varepsilon_{ij}}\frac{1}{\sum \frac{\partial A_{s,K}}{\partial \varepsilon_{ij}}} \tag{63}$$

$$\frac{\partial}{\partial\phi}\frac{\partial\mathcal{A}_K}{\partial\mathcal{A}} = \frac{\partial^2 A_{s,K}}{\partial\phi^2}\frac{1}{\sum\dfrac{\partial A_{s,K}}{\partial\phi}} - \frac{\partial A_{s,K}}{\partial\phi}\frac{\sum\dfrac{\partial^2 A_{s,K}}{\partial\phi^2}}{\left(\dfrac{\partial A_{s,K}}{\partial\phi}\right)^2} + \frac{\partial^2 A_{s,K}}{\partial\phi\,\partial\varepsilon_{ij}}\frac{1}{\sum\dfrac{\partial A_{s,K}}{\partial\varepsilon_{ij}}} + \frac{\partial A_{s,K}}{\partial\varepsilon_{ij}}\frac{\sum\dfrac{\partial^2 A_{s,K}}{\partial\phi\,\partial\varepsilon_{ij}}}{\sum\dfrac{\partial A_{s,K}}{\partial\varepsilon_{kl}}\sum\dfrac{\partial A_{s,K}}{\partial\varepsilon_{kl}}} \tag{64}$$

$$\frac{\partial}{\partial\varepsilon_{ij}}\frac{\partial\mathcal{A}_K}{\partial\mathcal{A}} = \frac{\partial^2 A_{s,K}}{\partial\phi\,\partial\varepsilon_{ij}}\frac{1}{\sum\dfrac{\partial A_{s,K}}{\partial\phi}} - \frac{\partial A_{s,K}}{\partial\phi}\frac{\sum\dfrac{\partial^2 A_{s,K}}{\partial\phi\,\partial\varepsilon_{ij}}}{\left(\sum\dfrac{\partial A_{s,K}}{\partial\phi}\right)^2} + \frac{\partial^2 A_{s,K}}{\partial\varepsilon_{ij}\,\partial\varepsilon_{kl}}\frac{1}{\sum\dfrac{\partial A_{s,K}}{\partial\varepsilon_{kl}}} + \frac{\partial A_{s,K}}{\partial\varepsilon_{kl}}\frac{\sum\dfrac{\partial^2 A_{s,K}}{\partial\varepsilon_{ij}\,\partial\varepsilon_{kl}}}{\sum\dfrac{\partial A_{s,K}}{\partial\varepsilon_{pq}}\sum\dfrac{\partial A_{s,K}}{\partial\varepsilon_{pq}}} \tag{65}$$